

UNIVERSIDADE FEDERAL DO RIO GRANDE DO SUL  
INSTITUTO DE INFORMÁTICA  
PROGRAMA DE PÓS-GRADUAÇÃO EM COMPUTAÇÃO

MATHEUS LUAN KRUEGER

**Visual Simulation of Refractive Errors on  
Monochromatic Images  
and  
An Empirical Evaluation of the Absolute  
Threshold for Vision**

Thesis presented in partial fulfillment  
of the requirements for the degree of  
Master of Computer Science

Advisor: Prof. Dr. Manuel Menezes de Oliveira Neto

Porto Alegre  
July 2015

## CIP — CATALOGING-IN-PUBLICATION

Krueger, Matheus Luan

Visual Simulation of Refractive Errors on Monochromatic Images  
and

An Empirical Evaluation of the Absolute Threshold for Vision /  
Matheus Luan Krueger. – Porto Alegre: PPGC da UFRGS, 2015.

81 f.: il.

Thesis (Master) – Universidade Federal do Rio Grande do Sul.  
Programa de Pós-Graduação em Computação, Porto Alegre, BR–  
RS, 2015. Advisor: Manuel Menezes de Oliveira Neto.

1. Visual blur. 2. Wavefront aberrations. 3. PSF. 4. Absolute  
threshold. I. Oliveira Neto, Manuel Menezes de. II. Título.

UNIVERSIDADE FEDERAL DO RIO GRANDE DO SUL

Reitor: Prof. Carlos Alexandre Netto

Vice-Reitor: Prof. Rui Vicente Oppermann

Pró-Reitor de Pós-Graduação: Prof. Vladimir Pinheiro do Nascimento

Diretor do Instituto de Informática: Prof. Luis da Cunha Lamb

Coordenador do PPGC: Prof. Luigi Carro

Bibliotecária-chefe do Instituto de Informática: Beatriz Regina Bastos Haro

*This thesis is dedicated to my parents,  
Marcilio Krueger and Ruth Matias Krueger,  
for their support, trust and unconditional love.*



## **ACKNOWLEDGMENTS**

This journey would not have been possible without the support of my family, professors and mentors, and friends. I would like to thank my family, for encouraging me in all of my pursuits and inspiring me to follow my dreams. To my friends, thank you for supporting and helping me over the years. I am also grateful to Manuel Menezes de Oliveira Neto e Airton Leite Kronbauer, my mentors, for their sincere and valuable guidance along this journey.

I take this opportunity to express my gratitude to Fundação de Amparo à Pesquisa do Estado do Rio Grande do Sul (FAPERGS) and Coordenação de Aperfeiçoamento de Pessoal de Nível Superior (CAPES) for financial support. I also place on record, my sense of gratitude to one and all, who directly or indirectly, have lent their ‘eyes’ in this venture.



## ABSTRACT

We present a practical approach to the problem of visual simulation of blur on monochromatic images. It uses Fourier Optics and a DSLR camera to simulate and validate results of how low-order aberrations (*i.e.*, myopia, hyperopia and astigmatism) affect vision. We demonstrate its effectiveness by comparing the simulation outcomes with an optical ground truth by using two objective metrics. In addition to simulation, we present a psychophysical study about the visual absolute threshold, suggesting its applicability in a more realistic rendering of how an individual perceives the environment. Preliminary evaluation has shown that our technique produces convincing results.

**Keywords:** Visual blur. Wavefront aberrations. PSF. Absolute threshold.





## **Simulação visual de borramento em imagens monocromáticas**

### **RESUMO**

Esta dissertação apresenta uma solução prática para o problema de simulação visual de borramento em imagens monocromáticas. Nossa técnica utiliza óptica de Fourier e uma câmera DSLR para simular e validar os resultados de como as aberrações de baixa ordem (miopia, hipermetropia e astigmatismo) afetam a visão. Nós demonstramos a sua eficácia utilizando duas métricas objetivas de comparação entre os resultados da simulação e imagens capturadas por uma câmera simulando o mesmo nível de aberração. Além da simulação, também apresentamos um estudo psicofísico a respeito do mínimo visível, sugerindo a sua aplicabilidade na renderização realística de como um indivíduo percebe o ambiente. Uma avaliação preliminar mostra que nossa técnica produz resultados convincentes.

**Palavras-chave:** Borramento visual, Aberrações de frente de onda, PSF, Mínimo visível.



## LIST OF FIGURES

Figure 1.1 The human eye and some low-order aberrations .....	17
Figure 1.2 A real scene with objects at different depths .....	19
Figure 2.1 General flow of sensory information .....	21
Figure 2.2 The Electromagnetic Spectrum and Visible Light.....	22
Figure 2.3 Human Senses: organs, energy stimuli, and sensory receptors .....	23
Figure 2.4 Construction of the optotype E.....	24
Figure 2.5 Parts of the Eye .....	25
Figure 2.6 The unit circle .....	26
Figure 2.7 Zernike terms expansion pyramid.....	28
Figure 2.8 General concepts of wavefront .....	29
Figure 3.1 Overview of the vision-realistic rendering algorithm.....	31
Figure 3.2 Yu (2001) uses data captured using a Shack-Hartmann aberrometer (a) to simulate blur at specific depth values (b) and (c). .....	33
Figure 3.3 The temporal glare pipeline .....	33
Figure 4.1 A roadmap for Fourier optics .....	35
Figure 4.2 Standard Sloan Letters.....	36
Figure 4.3 Example of a normalized Wavefront map .....	38
Figure 4.4 Typical eyeglasses' vertex distance of 12mm.....	38
Figure 4.5 Optical systems used in the validation process.....	40
Figure 4.6 Myopic perception of 20/200 Sloan black letters .....	41
Figure 4.7 Myopic perception of 20/200 Sloan white letters.....	42
Figure 4.8 Hyperopic perception of 20/200 Sloan black letters .....	43
Figure 4.9 Hyperopic perception of 20/200 Sloan white letters .....	44
Figure 4.10 Astigmatic perception of 20/200 Sloan black letters (-2 @ 90) .....	45
Figure 4.11 Astigmatic perception of 20/200 Sloan black letters (-2 @ 180) .....	46
Figure 4.12 Astigmatic perception of 20/200 Sloan white letters (+2 @ 90).....	47
Figure 4.13 Astigmatic perception of 20/200 Sloan white letters (+2 @ 180).....	48
Figure 4.14 ??? .....	49
Figure 4.15 ??? .....	50
Figure 4.16 Simulation of how lower and higher order visual aberrations affect the perception.....	51
Figure 5.1 Geometrical perspective of the circle of confusion .....	53
Figure 5.2 Absolute Threshold Experiment stages .....	54
Figure 5.3 Apparatus designed to help in the absolute threshold psychophysical evaluations .....	57
Figure 5.4 Variations of the apparatus .....	58
Figure 5.5 Plot of absolute threshold data acquired with and without eyedrops .....	58
Figure 5.6 Accommodation analysis.....	59
Figure 5.7 Polynomial fitting of the absolute threshold values of Individual 1 .....	60
Figure 5.8 Polynomial fitting of the absolute threshold values of Individual 11 .....	61



## LIST OF TABLES

Table 2.1	Sensory threshold of five senses.....	23
Table 2.2	Zernike polynomials up to the fifth order.....	27
Table 4.1	Camera apertures and pupil diameters for various f-numbers. ....	40
Table 4.2	SSIM and PSNR table of myopic perception (Figure 4.6).....	42
Table 4.3	SSIM and PSNR table of myopic perception (Figure 4.7).....	42
Table 4.4	SSIM and PSNR table of hyperopic perception (Figure 4.8).....	43
Table 4.5	SSIM and PSNR table of hyperopic perception (Figure 4.9).....	44
Table 4.6	SSIM and PSNR table of the negative astigmatic perception .....	45
Table 4.7	SSIM and PSNR table of the positive astigmatic perception .....	45



## CONTENTS

<b>1 INTRODUCTION.....</b>	<b>17</b>
1.1 Contributions.....	18
1.2 Thesis Structure .....	18
<b>2 BACKGROUND.....</b>	<b>21</b>
2.1 Sensation and Perception .....	21
2.2 Psychophysics .....	23
2.3 The Human Eye.....	24
2.3.1 Anatomy.....	24
2.3.2 Visual Aberrations .....	26
2.4 Optics and Wavefront Theory.....	28
2.4.1 Summary .....	29
<b>3 RELATED WORK .....</b>	<b>31</b>
3.1 Visual Simulation .....	31
3.1.1 Optical Simulation Techniques .....	31
3.1.2 Non-Optical Simulation Techniques.....	32
3.2 Estimating/Correcting Visual Optical Aberrations .....	33
<b>4 VISUAL SIMULATION OF REFRACTIVE ERRORS .....</b>	<b>35</b>
4.1 Target Images and Capture Setup.....	36
4.2 Modeling Visual Aberrations.....	37
4.2.1 Vertex Distance and Ray Transfer Matrix.....	38
4.3 Image Filtering.....	39
4.4 Validation.....	39
4.4.1 Comparison of Simulated Results with Ground Truth.....	40
<b>5 ABSOLUTE THRESHOLD .....</b>	<b>53</b>
5.1 Absolute Threshold .....	53
5.1.1 Experimental Design.....	54
5.1.2 Participants.....	55
5.1.3 Quasi-Random Algorithm.....	55
5.1.4 Simulation .....	56
5.2 Absolute Threshold .....	56
<b>6 CONCLUSION .....</b>	<b>63</b>
6.1 Future Work .....	63
<b>REFERENCES.....</b>	<b>65</b>
<b>APPENDIX A — INDIVIDUAL PARTICIPANT DATA .....</b>	<b>69</b>
<b>ANNEX A — EXAMPLE OF A SIMPLE OPTICAL SYSTEM.....</b>	<b>77</b>





## 1 INTRODUCTION

Vision is the primary channel we use to perceive the universe. Its unique capability allows us to acquire information about the surrounding world by sensing the intensity and color of light. This experience is unique and the perceived image is affected by several individual factors (*e.g.*, refractive errors, light sensitivity, distribution of photoreceptors in the retina, etc.). Simulating visual experience is a complex and difficult task, which requires the integration of a wide range of fields, including optics, anatomy, physiology, biochemistry, psychology, and cognitive neurosciences (SCHWARTZ, 2010).

Visual aberrations can be classified as low-order or high-order. Low-order aberrations (*i.e.*, myopia, hyperopia, astigmatism, and presbyopia) can be described in terms of spherocylindrical values and can be corrected with the use of eye glasses, contact lenses, or refractive surgery. They are responsible for about 90% of one's loss of visual acuity (DIAS-SANTOS et al., 2014). The remaining 10% is due to a combination of particular imperfections, known as high-order aberrations (*e.g.*, trefoil, coma, quadrafoil, secondary astigmatism). Visual aberrations can be described by the eye's point-spread function (PSF), often represented using the so-called wavefront maps. Figure 1.1 illustrates the human eye and the effects of some low-order aberrations when focusing at infinity.

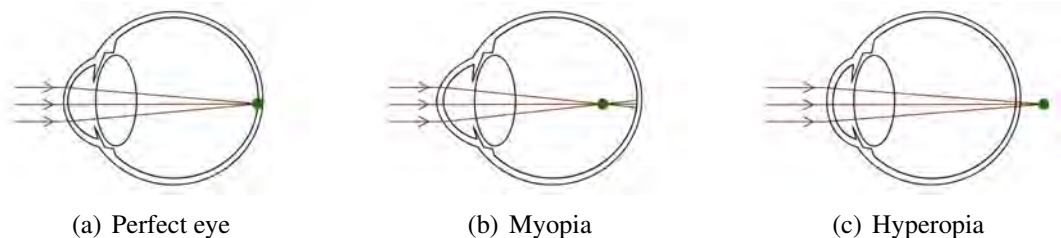


Figure 1.1 – The human eye and some low-order aberrations. (a) A perfect eye focuses the parallel rays to a single point on the retina; (b) a myopic eye has an elongated eye ball or a bumped cornea, focusing parallel rays at a point before the retina; (c) a hyperopic eye has a shallow eye ball or a flatter cornea, thus focusing parallel rays at point behind the retina (modified from (PAMPLONA et al., 2010)).

The simulation of how an impaired eye perceives a scene is a complex, but highly important task. It could, for instance, give doctors an idea of how a given patient's vision was before and after some surgical procedure. It could also allow primary school teachers understand the complaints of their students. In practice, poor visual performance is often misinterpreted as the perception of blurry images. However, the problem is not that simple. Visual simulation is an intricate process that requires sophisticated tools of Fourier analysis (THIBOS; THIBOS, 2011). From a simple geometrical perspective, when the optical system of an eye is mis-focused at a point in the scene, the light emitted/reflected by such a point is spread out across some area

(circle of confusion) of the retinal surface, causing blur. This can be understood from Figures 1.1(b) and 1.1(c), and observed in Figure 1.2(c), which was captured using a myopic camera. Note that when the optical system is well focused (Figure 1.1(a)) a point on the scene is imaged to a point on the retina.

Unlike traditional 2-D digital image processing in which an image is blurred by convolving it with a spatially-invariant low-pass filter kernel (Figure 1.2(b)), visual blurring is a depth-dependent phenomenon (*i.e.*, the amount of blurring introduced by the eye's PSF varies with the distance from the observer's focal plane to the scene element). If depth is not taken into account by the blurring method, the resulting image might be very different from the one formed onto the retina — Figure 1.2(c).

We present a practical approach to the problem of visual simulation of blur on monochromatic images. Our approach uses Fourier Tools and a camera to simulate and validate results of how low-order aberrations affect vision.

## 1.1 Contributions

The main **contributions** of this thesis include:

- A technique to perform visual blurring;
- A schematic eye model that mimics a DSLR camera's perception;
- A database of Sloan letter images for testing vision at 3 feet;
- Psychophysical experiments involving the absolute threshold.

## 1.2 Thesis Structure

The remaining of this thesis is organized as follows: Chapter 2 reviews the theoretical basis for the further anatomical, optical, and numerical discussions. Chapter 3 discusses previous visual simulation techniques, as well as methods for estimating optical aberrations. It also discusses simulation techniques that take non-optical characteristics into account. Chapter 4 presents our approach for visual simulation of blur on monochromatic images. Additionally, it explains how the technique can be combined with the minimum amount of light perceived by an individual. Chapter 5 presents our results. Finally, Chapter 6 summarizes this thesis and suggests some ideas for future work.



(a)



(b)



(c)

Figure 1.2 – A real scene with objects at different depths. (a) Photograph taken with a DSLR camera, with all objects in focus; (b) result of convolving the photograph in (a) with a 2-D low-pass filter. ( $\sigma = 15$ ); (c) Adding an extra lens (+1 diopter) to the camera's optical system to simulate myopia. Note how the amount of blurring increases with distance.



## 2 BACKGROUND

The study of how optical aberrations affect visual experience requires a more thorough understanding of human perception and the wave properties of light. In this chapter, we establish and review some of the theoretical principles that were used in the experimental studies, data analysis, interpretation of the results.

### 2.1 Sensation and Perception

Sensation and perception are the processes that put us in contact with stimuli from our world — objects and events (KING, 2012). Understanding these processes requires comprehending the physical properties of our perception and the study of the corresponding sensor, for example, light and the eye. Lemma (2005) defines some concepts that are necessary to explain how stimulation (*e.g.*, visual information) becomes meaningful perception: (i) *stimulus*: a source of physical energy that produces a response in a sense organ; (ii) *response*: any reaction of an organism to or in the presence of a stimulus; (iii) *transduction*: sequence of operations by which physical energy is transformed into patterns of neural impulses that give rise to sensory experience; (iv) *sensation*: process of receiving stimulus energies from external environment and transforming those energies into neural energy; and (v) *perception*: process whereby the brain interprets sensations, taking into account past experiences, the context in which the sensation occurs, and emotions.

The steps related to the perception of a visual information are illustrated in Figure 2.1, where light waves reflected from the butterfly act as stimuli to react with our sensory receptors, which convert the energy into neural signals. After that, neural messages travel to the sensory cortex of the brain and become sensations. Finally, the process of perception interprets these sensations and grant us to recognize a butterfly (ZIMBARDO; JOHNSON; MCCANN, 2012).

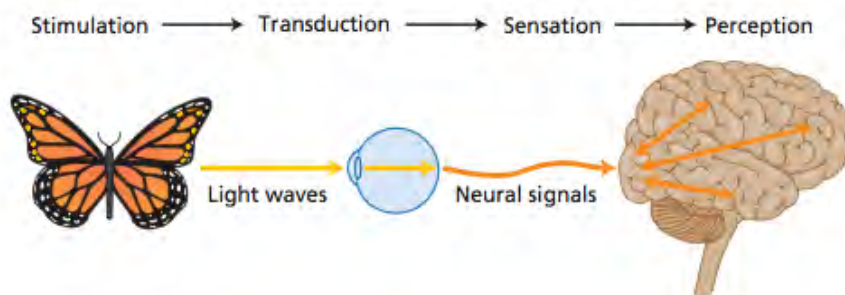


Figure 2.1 – General flow of sensory information from energy stimulus to sensory receptor cell to sensory neuron to sensation and perception (ZIMBARDO; JOHNSON; MCCANN, 2012).

Light is a form of electromagnetic (EM) radiation which travels through space in waves and can be described in terms of its physical characteristics — wavelengths and/or amplitude. Color and brightness are the psychological counterparts of light wavelength and intensity that exist only in the brain (KING, 2012). Humans are capable of detecting only a tiny segment of the EM spectrum, called visible light (Figure 2.2), which ranges in wavelength from approximately 400 to 700 nm ( $1\text{nm} = 10^{-9}\text{m}$ ). Wavelengths outside this range are not detected by humans because they are not transmitted by the ocular media or cannot be absorbed by our retinal photopigments Schwartz (2010).

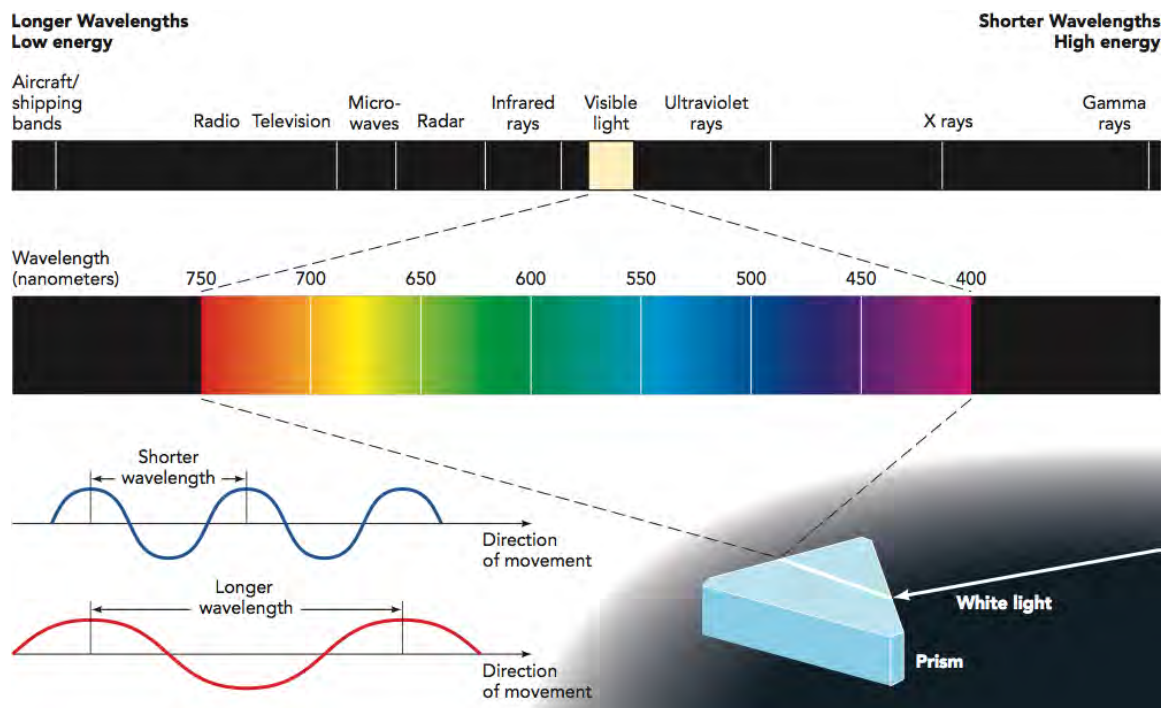


Figure 2.2 – The Electromagnetic Spectrum and Visible Light: (Top) Visible light is only a narrow band in the electromagnetic spectrum. Visible light wavelengths range from 400 to 700 nanometers. X rays are much shorter, radio waves much longer. (Bottom) The two graphs show how waves vary in length between successive peaks. Shorter wavelengths are higher in frequency, as reflected in blue colors; longer wavelengths are lower in frequency, as reflected in red colors (KING, 2012).

Distinct neural messages flows into the nervous system as information, and it's type depends on the energy captured by a sensory receptor. Figure 2.3 shows the human sensory receptors for vision, hearing, touch, smell, and taste. In order to generate a sensory experience from any receptor, there is a minimal amount of physical energy needed - known as absolute threshold (ZIMBARDO; JOHNSON; MCCANN, 2012).

Table 2.1 shows some typical absolute threshold levels for several familiar stimuli. Experiments designed to determine thresholds, and the study of the relationship between physical nature of stimuli and people's response to them belong to a branch of psychology called *psychophysics* (LEMMA, 2005).

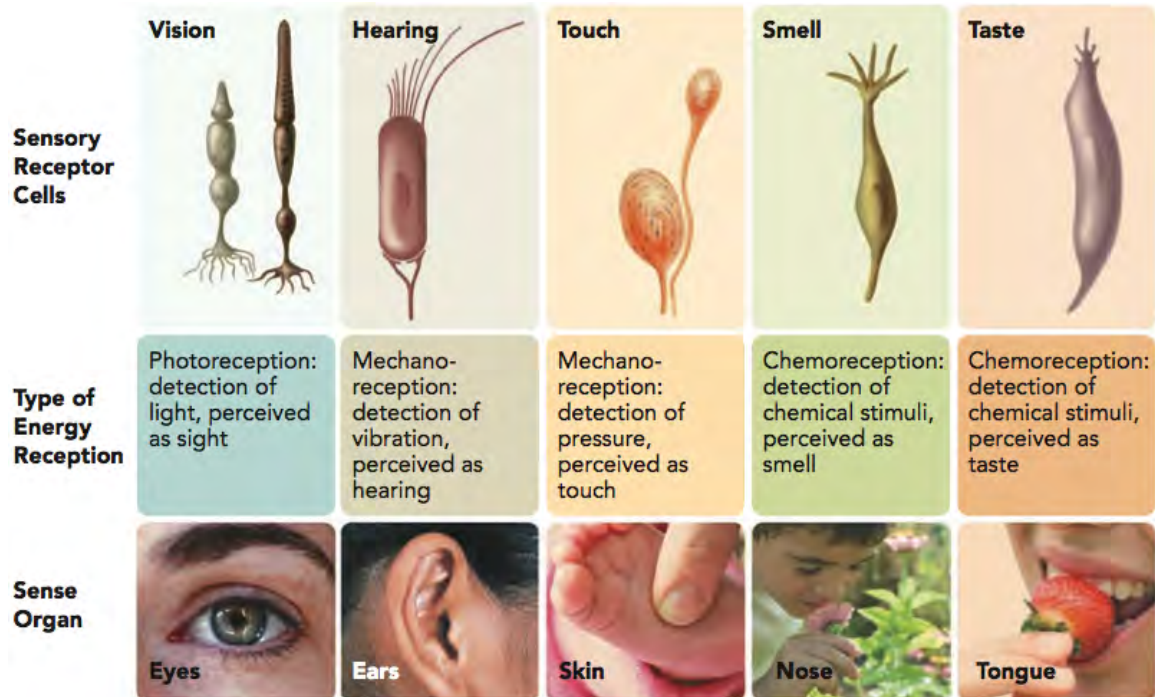


Figure 2.3 – Human Senses: organs, energy stimuli, and sensory receptors (KING, 2012).

Table 2.1 – Sensory threshold of five senses (ZIMBARDO; JOHNSON; MCCANN, 2012).

Sense	Detection Threshold
Sight	A candle flame at 30 miles on a clear, dark night
Hearing	The tick of a watch 20 feet away in a quiet room
Smell	One drop of perfume diffused throughout a three-room apartment
Taste	One teaspoon of sugar in 2 gallons of water
Touch	A bee's wing falling on the cheek from 1 centimeter above

## 2.2 Psychophysics

The term *psychophysics* was invented in 1860 by Gustav Theodor Fechner, a German physicist and philosopher, as a mathematical approach to relate mental and physical events on the basis of experimental data (TREUTWEIN, 1995). Generally, all sensory systems are able to detect varying degrees of energy, and psychophysical experiments frequently involve the determination of some absolute threshold. This is a complicated task because humans are not perfect observers. Lemma (2005) emphasizes that the thresholds determined by experiments or clinical procedures may be influenced by several factors, including decision criteria, attention, motivation, and internal neural noise. Further details about Fechner's original methods for determining absolute thresholds and some recent improvements are discussed in (KLEIN, 2001; LEEK, 2001; BLAKE; SEKULER, 2005).



## 2.3 The Human Eye

The eye is a sophisticated imaging system capable of dynamically adjusting its refractive power to focus at a wide range of depths. Optical aberrations in this imaging system are the main causes of loss of visual acuity. *Visual acuity* (*i.e.*, the eye's ability to see fine details) can be determined with an auxiliary chart, in which the individual must resolve its details (*e.g.*, bars and gaps) to recognize targets, such as Snellen or Sloan letters (Figure 2.4). The ability to distinguish between two details determines the *Minimum Angle of Resolution* (MAR). The standard visual acuity for humans is 1 arc minute (one-sixtieth of one degree) (SCHWARTZ, 2010). In ophthalmology, visual acuity is commonly recorded in the form of the *Snellen fraction*:  $VA = D'/D$ , where  $D'$  is the standard viewing distance (usually 20 feet) and  $D$  is the distance at which each letter in the chart line subtends 5 arc minutes. The larger the  $D$  value, the worse the vision. The term 20/20 vision is the standard for emmetropes (*i.e.*, at a 20 feet distance, a person with normal vision should be able to read the small 20/20 line on an eye chart).

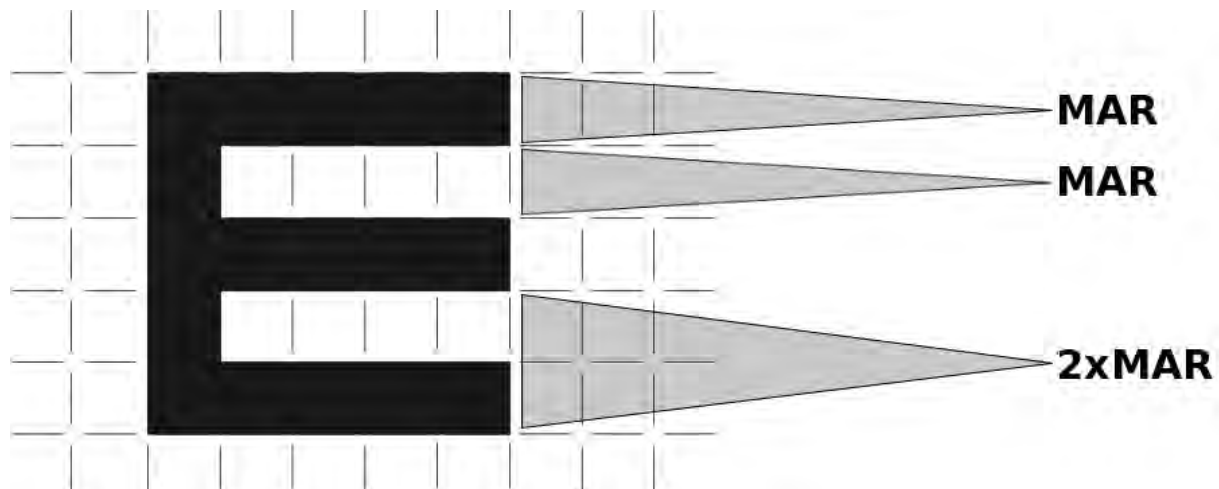


Figure 2.4 – Construction of the optotype E. The detail (a bar or a gap) is one-fifth of the overall size of the optotype. MAR stands for Minimum Angle of Resolution, which corresponds to 1 arc minute. Modified from Schwartz (2010).

### 2.3.1 Anatomy

The human eye is constituted of several tissues, which contains approximately 126 million receptors cells (KING, 2012). It can be divided into three concentric layers and two chambers, plus the iris, pupil, and lens. In an adult, it has an average length of 25.4 mm. The



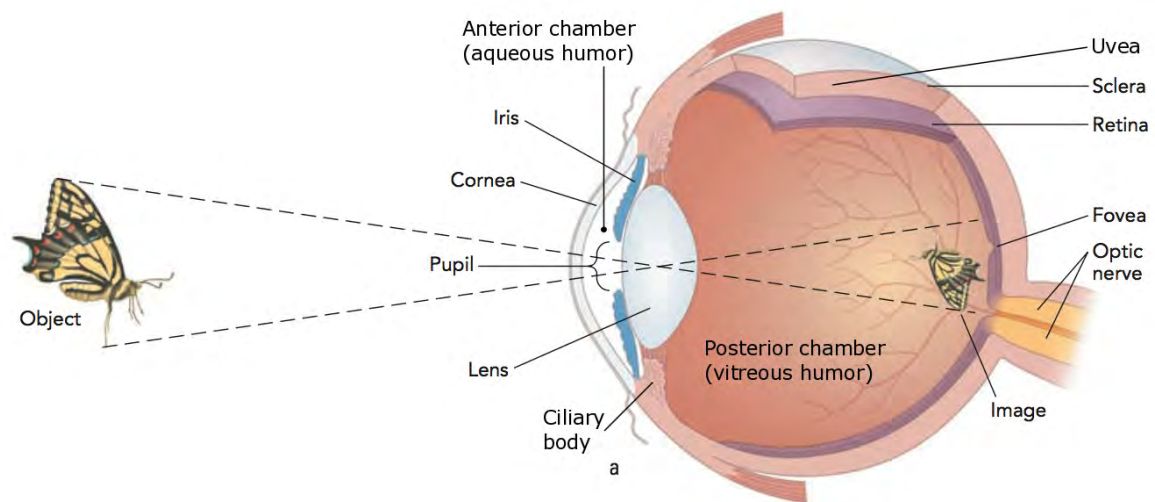


Figure 2.5 – Parts of the Eye. Note that the image of the butterfly on the retina is upside down. The brain allows us to see the image right side up. (modified from King (2012)).

outermost layer is the *sclera*, the middle layer is the *uvea*, and the innermost layer is the *retina*. Figure 2.5 shows a cross section an a human eye and its parts.

The sclera averages about 1 millimeter in thickness and is made of tightly packed, interwoven fibers that guarantee its toughness. The sclera needs to be tough due to eyeball's pressure, which is the double of the atmospheric pressure (BLAKE; SEKULER, 2005). There is a transparent membrane at the very front of the eye, called *cornea*. The cornea is responsible for two-thirds (40 diopters) of the eye's refractive power (total power of 60 diopters) (TKACZYK, 2010). Most part of the uvea layer consists of a heavily pigmented, spongy structure called the *choroid*. The choroid averages 0.2 mm thick and contains a network of blood vessels, including capillaries, for blood supply. Its pigmentation reduces light scattering by capturing light that is not captured by the retinal receptor cells. According to King (2012), the "retina is a light-sensitive surface that records electromagnetic energy and converts it to neural impulses for later processing". It has two kinds of photoreceptors (*i.e.*, light sensitive receptors cells): rods and cones. The retina resembles a very thin, fragile meshwork, which explains its name — *rete* is Latin for "fisherman's net" (BLAKE; SEKULER, 2005).

Both anterior and posterior chambers contains a specific humor (Figure 2.5), which is a transparent liquid continuously produced by the ciliary body. Both aqueous and vitreous humors serve a number of important functions, as maintain the eyeball's shape and nourishment. The iris is the circular section of tissue that gives the eye its characteristic color: brown, blue, green, etc. In the middle of the iris there is the pupil, whose size varies according to the illumination level with the help of two sets of muscles — the inner and radial (SCHWIEGERLING, 2004). Its average diameter varies from 2 millimeters to 8 millimeters, and depends on several factors,

such as individual characteristics and luminance level (YODER; VUKOBRATOVICH, 2011).

Right behind the iris, lies an important optical element of the eye, the crystalline lens (see Figure 2.5). A gradient-refractive-index lens that contributes approximately one-third (20 diopters) of the dioptric power of the eye, and modifies its shape to focus on near or distant objects (SCHWIEGERLING, 2004). This variation, from nearly flat to rounder, causes changes in the final optical power and is called *accommodation*. Through accommodation, the lens can correctly focus on the retina the light coming from the scene. For good vision, the crystalline lens must be transparent. Loss of transparency, known as *cataracts* leads to a decrease in vision quality (SCHWARTZ, 2010).

### 2.3.2 Visual Aberrations

Visual aberrations are the main cause of visual impairment. Estimates indicate that there are about 153 million people with visual impairment due to uncorrected refractive errors (WHO, 2007). Thibos et al. (2002) defined standards for reporting of optical imperfections of eyes. The method of choice for assessing eye aberrations (*i.e.*, describing its wavefront aberration) are the so called *Zernike polynomials*. They consist of a series of orthogonal polynomials over the area of a unitary circle (Figure 2.6) and can be expressed either in Cartesian ( $X, Y$ ) or polar ( $\theta, \rho$ ) coordinate systems. The conversions between the two are given by:

$$\begin{aligned} \rho &= \sqrt{x^2 + y^2} & \theta &= \tan^{-1}(y/x) \\ x &= \rho * \cos \theta & y &= \rho * \sin \theta \end{aligned} \tag{2.1}$$

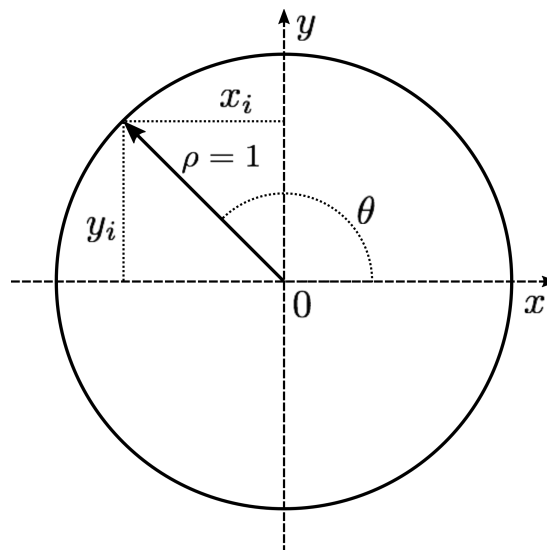


Figure 2.6 – The unit circle.

There are several different normalization and numbering schemes for representing Zernike polynomials. Here we adopt a double indexing scheme ( $Z_n^m$ , where  $n$  is the *order* and  $m$  is the *frequency* – see Figure 2.7). Such a scheme is defined as:

$$Z_n^m(\rho, \theta) = \begin{cases} N_n^m R_n^{|m|}(\rho) \cos m\theta, & \text{for } m \geq 0, \\ -N_n^m R_n^{|m|}(\rho) \sin m\theta, & \text{for } m < 0, \end{cases}$$

where  $N_n^m$ ,  $R_n^{|m|}$  and the sinusoidal functions stand for the normalization factor, radial component, and azimuthal component, respectively. Such terms are fully described by Thibos et al. (2002). Some of the *Zernike polynomials* (up to the 5<sup>th</sup> order) are listed in Table 2.2 and illustrated in Figure 2.7. They can be applied directly to wavefront evaluation in the eye's pupil. In ophthalmology, the radial degree  $n$  is the basis for classifying aberrations as lower-order ( $n \leq 2$ ) and higher-order ( $n > 2$ ). [Piston nao eh aberracao, certo? logo temos que verificar a notacao para sermos precisos.](#)

Table 2.2 – Zernike polynomials up to the fifth order.

j	n	m	Zernike Polynomials	Name
0	0	0	1	piston
1	1	-1	$2\rho \sin \theta$	vertical tilt
2	1	1	$2\rho \cos \theta$	horizontal tilt
3	2	-2	$\sqrt{6}\rho^2 \sin \theta$	oblique astigmatism
4	2	0	$\sqrt{3}(2\rho^2 - 1)$	defocus
5	2	2	$\sqrt{6}\rho^2 \cos \theta$	vertical astigmatism
6	3	-3	$\sqrt{8}\rho^3 \sin 3\theta$	vertical trefoil
7	3	-1	$\sqrt{8}(3\rho^3 - 2\rho) \sin \theta$	vertical coma
8	3	1	$\sqrt{8}(3\rho^3 - 2\rho) \cos \theta$	horizontal coma
9	3	3	$\sqrt{8}\rho^3 \cos 3\theta$	oblique trefoil
10	4	-4	$\sqrt{10}\rho^4 \sin 4\theta$	oblique quadrafoil
11	4	-2	$\sqrt{10}(4\rho^4 - 3\rho^2) \sin 2\theta$	oblique secondary astigmatism
12	4	0	$\sqrt{5}(6\rho^4 - 6\rho^2 + 1)$	primary spherical
13	4	2	$\sqrt{10}(4\rho^4 - 3\rho^2) \cos 2\theta$	vertical secondary astigmatism
14	4	4	$\sqrt{10}\rho^4 \cos 4\theta$	vertical quadrafoil
15	5	-5	$\sqrt{12}\rho^5 \sin 5\theta$	vertical pentafoil
16	5	-3	$\sqrt{12}(5\rho^5 - 4\rho^3) \sin 3\theta$	vertical secondary trefoil
17	5	-1	$\sqrt{12}(10\rho^5 - 12\rho^3 + 3\rho) \sin \theta$	vertical secondary coma
18	5	1	$\sqrt{12}(10\rho^5 - 12\rho^3 + 3\rho) \cos \theta$	horizontal secondary coma
19	5	3	$\sqrt{12}(5\rho^5 - 4\rho^3) \cos 3\theta$	oblique secondary trefoil
20	5	5	$\sqrt{12}\rho^5 \cos 5\theta$	oblique pentafoil

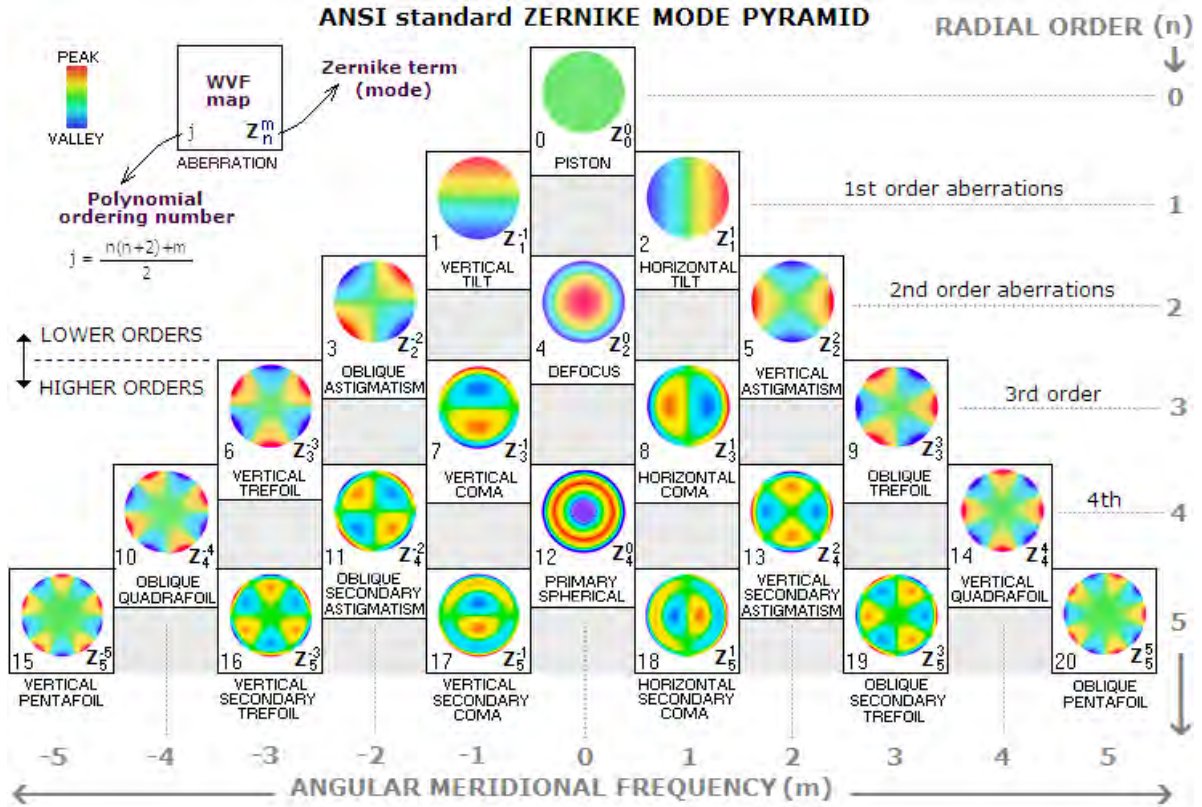


Figure 2.7 – The Zernike expansion pyramid: a function of term's radial degree (or order)  $n$  and azimuthal frequency  $m$  (SACEK, 2015).

## 2.4 Optics and Wavefront Theory

The human eye consists of several optical components, notably the cornea, the crystalline lens, the pupil, and the retina. Visual aberrations are the combination of the imperfections/anomalies from the outermost to the innermost component. The aim of vision correction is to remove or to minimize the ocular aberrations of the visual system. But to achieve this goal, we first need to understand and analyze how light behaves inside the eye.

According to Sacek (2015) even though *geometrical optics* provides a proper way of determining image location and magnification by tracking paraxial rays, the determination of optical systems' aberrations require more complex calculation considering light waves and its propagation (*i.e.*, *physical optics*).

Dai (2008) states that "a propagating wavefront can be characterized as many rays propagating in different directions as determined by the local slopes of the wavefront surface". Suppose there is an original wavefront  $W(x, y)$ , centered at point  $O$  and conformed within the aperture  $\Sigma$ , as shown in Figure 2.8(a). When it propagates towards an eye by a distance  $d$ , it becomes

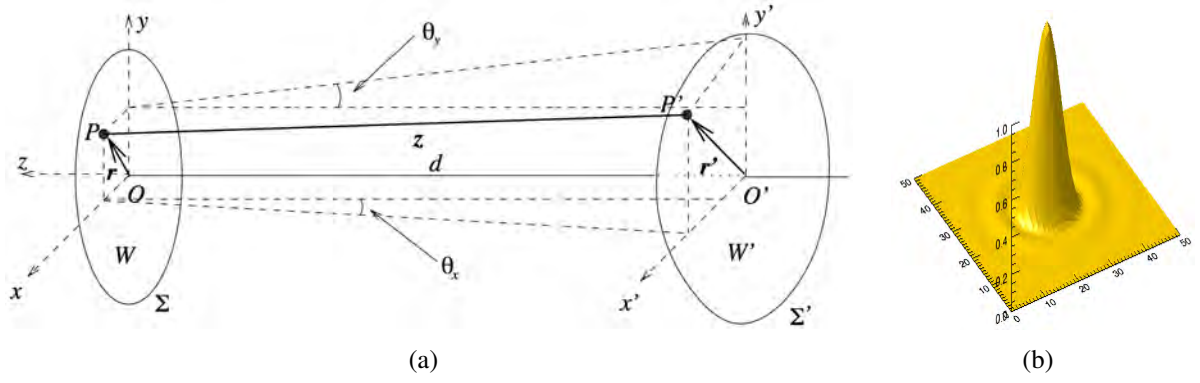


Figure 2.8 – General concepts of wavefront: (a) Geometry of the wavefront propagation (DAI, 2008); (b) the PSF generated by an aberrated wavefront (SMITH, 2015).

a new wavefront  $W'(x', y')$  given as

$$W'(x', y') = W(x, y) + z(x, y; x', y'), \quad (2.3)$$

where  $z(x, y; x', y')$  is the distance between points  $P(x, y)$  and  $P'(x', y')$  (Figure 2.8(a)), and can be written as:

$$z(x, y; x', y') = \sqrt{d^2 + (x - x')^2 + (y - y')^2}. \quad (2.4)$$

The propagation of a wavefront  $W(x, y)$  consisting of low-order aberrations only, expressed with Zernike Polynomials, is discussed by (DAI, 2008). In addition, the author discusses several optical metrics of ocular wavefronts. A very good predictor for visual performance is the point spread function (PSF), which describes how a ray of light is dispersed in a given space. It is represented by a 2-D array and, as shown in Figure 2.8(b), resembles a surface in 3-D. It can be obtained using Fourier Optics (GOODMAN, 2005) and the eye's wavefront aberration information.

### 2.4.1 Summary

This chapter reviewed the background information about the human eye required for understanding the remaining of this thesis.



### 3 RELATED WORK

Vision simulation has been addressed in different ways over the years. Since the first synthetic image with depth of field computed by Potmesil and Chakravarty (1981), there has been a significant number of computer graphics techniques addressing the rendering of realistic effects. More recently, the possibility of estimating and compensating for refractive errors has attracted the attention of several researchers, mainly addressing the formulation of interactive, portable, and inexpensive solutions. The following subsections describe the main techniques for simulating, estimating, and correcting visual aberrations.

#### 3.1 Visual Simulation

##### 3.1.1 Optical Simulation Techniques

Barsky (2004) proposed a method for generating synthetic images incorporating the optical characteristics of an individual. Specifically, his method simulates the perception of an individual based on data acquired using a Shack-Hartmann wavefront aberrometer. Figure 3.1 shows a rendered image using his technique, along with an overview of the algorithm. Note that once the wavefront data is captured, it is sampled to calculate an *Object Space PSF* (OSPSF) and used to blur the input synthetic scene at different depths.

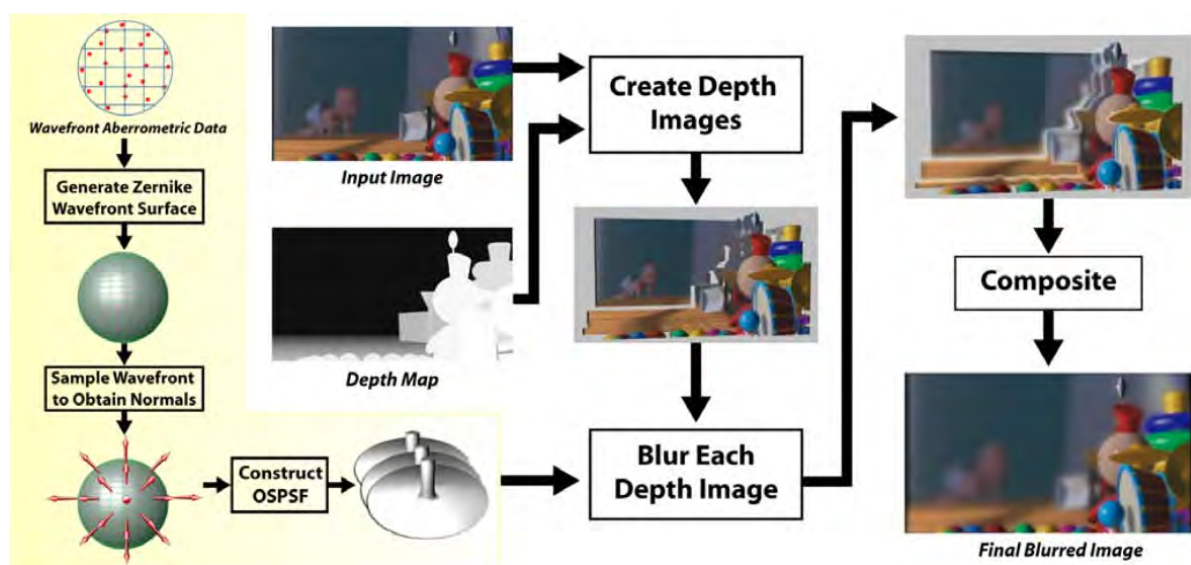


Figure 3.1 – Overview of the vision-realistic rendering algorithm proposed by Barsky (2004). Given an individual’s wavefront data and some synthetic scene, one can generate millions of samples necessary to calculate an OSPSF; create a set of depth images; blur each depth image; and composite them to obtain a final blurred image.



Many researchers have used raytracing techniques and anatomical optics to study and simulate vision by using theoretical models of the human eye (CAMP; MAGUIRE; ROBB, 1990; KOLB; MITCHELL; HANRAHAN, 1995). Camp, Maguire and Robb (1990) described two ray tracing algorithms for deriving an optical PSF from corneal topography measurements. They focused on simulating and evaluating optical performance of patients' eyes with the following corneal pathologies: *keratoconus*, *epikeratophakia for aphakia* and *radial keratotomy*. Kolb, Mitchell and Hanrahan (1995) presented a physically-based camera model that simulates aberration and radiation. To simulate such effects, they compute the geometry of image formation of a particular lens system using a modified distributed ray tracing algorithm. The algorithm is a hybrid of rendering and lens maker techniques, and can produce images of synthetic scenes showing a variety of optical effects. Mostafawy, Kermani and Lubatschowski (1997) combined the algorithm presented by Kolb, Mitchell and Hanrahan (1995) and the dimensions of an schematic eye model to generate virtual simulations of vision after corrective surgery.

Moreover, the study of monochromatic aberrations of the human eye with wavefront sensors (LIANG et al., 1994) allowed many others to perform simulations by using Fourier tools to mimic visual perception. Yu (2001) presents a technique capable of generating simulations of synthetic and real scenes focusing at a specific depth (Figures 3.2(b) and 3.2(c)). Instead of considering only the corneal surface and using raytracing techniques to perform such simulations, the authors rely on data captured by a Shack-Hartmann device (Figure 3.2(a)). With this information they construct a wavefront, which is used to blur a sharp image according to a depth map. However, they do not present a proper way of evaluating the simulations' outcomes, which could be, for example, compared with an optical ground truth. Watson and Ahumada Jr (2008) have used Fourier Optics and synthetic Sloan letters to establish a metric capable of predicting visual acuity from wavefront aberrations. [Descrva como eh esta metrica? Eles fizeram o mesmo que nos? Como o trabalho descrito nesta dissertacao se diferencia do deles?](#)

### 3.1.2 Non-Optical Simulation Techniques

Some techniques are concerned with modeling the effects caused by non-optical issues and use them to achieve more realistic synthetic images. One example is the method proposed by Deering (2005). His approach describes a retinal photon-accurate model of the human eye. Such a model is used together with computer graphics techniques and a simplified eye's optical model to produce synthetic simulations of the image formation process.

Another technique that explores different effects caused by the anatomy of the human



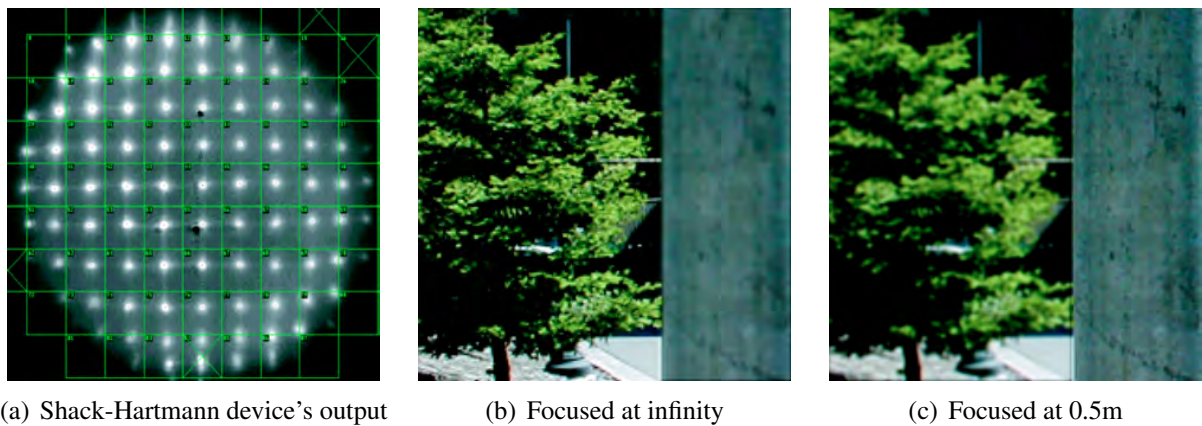


Figure 3.2 – Yu (2001) uses data captured using a Shack-Hartmann aberrometer (a) to simulate blur at specific depth values (b) and (c).

eye — the glare — is discussed by Ritschel et al. (2009). The authors proposed a model for a real-time dynamic simulation of the scattering in the human eye (Figure 3.3), which is efficiently implemented by drawing a few basic primitives, applying an FFT, and doing a special kind of blur. They have also performed psychophysical studies to measure the perception of brightness for glare models. However, they state that, as any other intrinsic phenomena, no ground truth can be obtained. And the model's validation remains a challenging task.

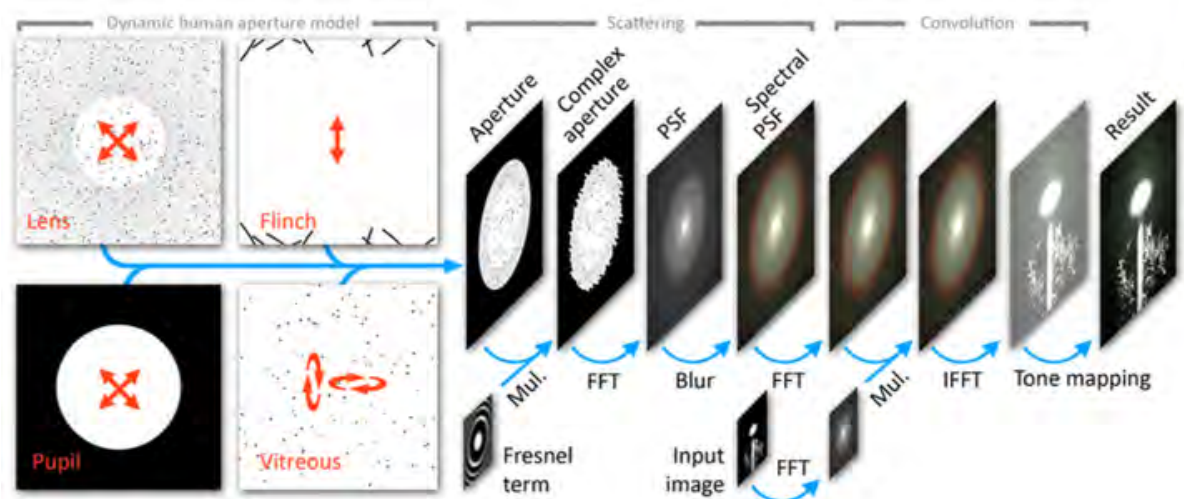


Figure 3.3 – The temporal glare pipeline (RITSCHER et al., 2009).

### 3.2 Estimating/Correcting Visual Optical Aberrations

Pamplona et al. (2010) presented a practical approach for estimating low-order aberrations without the need of expensive equipments. It uses a pinhole mask attached to a smartphone displaying patterns to the subject. The aberrations are estimated by the subjective alignment of

the different patterns. Kronbauer et al. (2011) developed a psychophysical approach for vision measurement in candelas. It consists in presenting light stimulus in a display in order to discover the absolute threshold for clear and dark conditions. Then, by relating it with an objective vision's assessment (*e.g.*, vision chart acuity and aberrometry data), they have stated a strong correlation between aberrometry data and the absolute threshold.

Many methods have achieved the goal of free the viewer from needing wearable optical correction when looking at displays (HUANG et al., 2012; PAMPLONA et al., 2012; HUANG et al., 2014), and printings or projections (MONTALTO et al., 2015). Other works have explored physiologically-based models to provide insights and feedback on how to produce high-fidelity effects and improve visualization experiences (MACHADO; OLIVEIRA; FERNANDES, 2009; PAMPLONA; OLIVEIRA; BARANOSKI, 2009; PAMPLONA et al., 2011).

## 4 VISUAL SIMULATION OF REFRACTIVE ERRORS

This chapter describes the approach used for visual simulation of low-order refractive errors. Figure 4.1 illustrates its pipeline, showing equivalent operations specified both in the spatial and in the frequency domain. Since we are primarily interested in visual acuity, all experiments and discussions presented here are based on monochromatic images. As visual blurring is a depth-dependent phenomenon, we have adopted the simplifying assumption that the observed images are at some constant depth. For this, we used two sets of charts containing standard Sloan letters (Figure 4.2): black letters on white background, as well as white letters on black background. The following sections provide the details of each step.

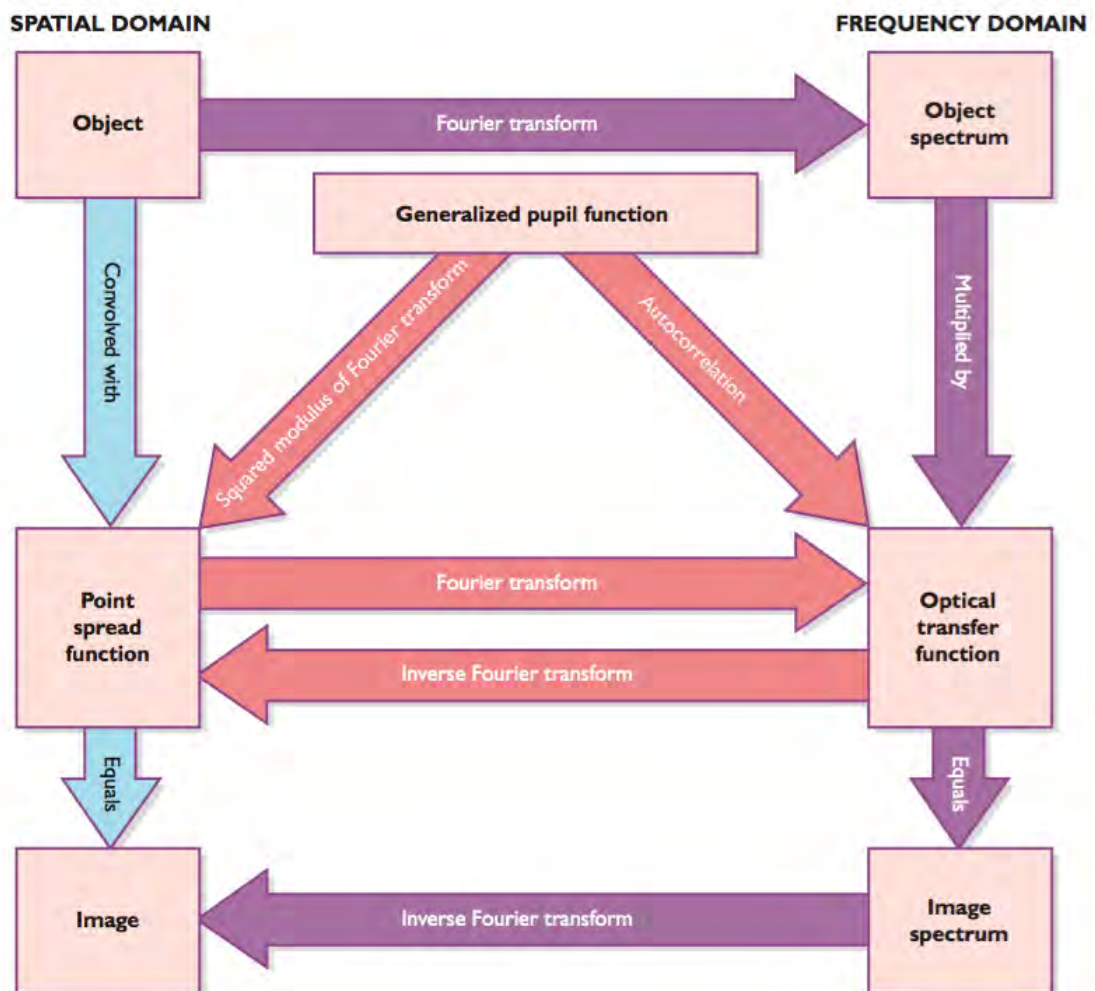


Figure 4.1 – The pipeline for simulating visual aberrations. In the spatial domain one needs the eye’s point spread function (PSF), whereas in frequency domain the optical transfer function (OTF) is required (MOLLON, 2003).



Figure 4.2 – Standard Sloan Letters.

#### 4.1 Target Images and Capture Setup

We have created images of Sloan letters at LogMAR values ranging from -0.3 to 1.0 in steps of 0.1. The LogMAR (Logarithm of the Minimum Angle of Resolution) scale (BAILEY; LOVIE, 1976) provides a more accurate estimate of visual acuity when compared to other charts (*e.g.*, Snellen), being the recommended one for research settings. Our target images were created for testing vision at 3 feet using Equation 4.1. The individual letters were rendered using the vector graphics capabilities of Inkscape and the Sloan PostScript fonts provided by Pelli, Robson et al. (1988). For each standard Sloan letter we generated files with 90 (@1x) and 360 (@4x) dpi, containing black letters on white background (Figure 4.2) as well as white letters on black background. At the prescribed distance, the ratio between one pixel and one arc minute is 1:1, that is, the letters with a LogMAR value of 0 (or the known Snellen fraction 20/20) has exactly 5 pixels of height. For the purpose of our simulations, each white (black) optotype was placed against a  $113 \times 133$ -pixel black (white) square. Since  $1 \text{ degree} = 60 \text{ arc minutes}$ , each such square covers a total field of view (FOV) of  $1,88^\circ \times 1,88^\circ$ . The LogMAR conversion to Snellen decimal values is presented in Equation 4.2.

$$letter \ size_{mm} = \left\{ \tan \left[ \text{deg2rad} \left( \frac{5}{60} \right) \right] \times (chart \ distance_{mm}) \times (10^{-\text{LogMAR}})^{-1} \right\} \quad (4.1)$$

$$\text{LogMAR} = -\log_{10}(\text{Snellen Decimal Acuity}) \quad (4.2)$$

We have printed the described LogMAR charts (containing Sloan letters specifically designed for 3 feet distance) using a laser printer. We then took pictures of the charts with a

DSLR camera. The camera was placed at 3 feet (91.44 cm) from the chart, with focal length set to 18mm. Since images acquired using this setup respect the 1:1 ratio between pixels and arc minutes, one can crop the squares containing the individual optotypes for further processing.

## 4.2 Modeling Visual Aberrations

We characterize the optical aberrations of the human eye using a wavefront aberration function. Such a function defines a wavefront map, which is approximated using a series of polynomials, such as the Zernike polynomials (see Section 2.3.2). Obtaining a complete wavefront function, which models both low-order and high-order aberrations, requires access to expensive wavefront aberrometer devices. In this work, we only consider the low-order aberrations (*i.e.*, myopia, hyperopia, and astigmatism), which can be easily obtained from any eyeglass or contact lens prescription. One should note, however, that low-order aberrations are responsible for about 90% of one's total visual aberrations (DIAS-SANTOS et al., 2014). This should not come as a surprise, given that eyeglasses only correct for low-order aberrations and are the primary way of achieving corrected 20/20 vision. We obtain wavefront aberration function  $W_{(x,y)}$  from prescription data as (DAI, 2008):

$$W_{(x,y)} = \sum_{i=-1}^1 c_2^{2i} Z_2^{2i}(x,y), \quad (4.3)$$

where

$$c_2^{-2} = \frac{R^2 * C * \sin(2\phi)}{4\sqrt{6}}, \quad (4.4)$$

$$c_2^0 = -\frac{R^2 * (S + C/2)}{4\sqrt{3}}, \quad (4.5)$$

$$c_2^2 = \frac{R^2 * C * \cos(2\phi)}{4\sqrt{6}} \quad (4.6)$$

and  $c_2^{-2}$ ,  $c_2^0$ , and  $c_2^2$  are the coefficients of the Zernike polynomials corresponding to *oblique astigmatism* ( $Z_2^{-2}$ ), *defocus* ( $Z_2^0$ ), and *vertical astigmatism* ( $Z_2^2$ ), respectively (see Figure 2.7).  $S$ , and  $C$  are respectively the *sphere* and *cylinder* values that specify the optical power in diopters (D).  $\phi$  is cylinder axis expressed in degrees.  $R$  is the radius of the subject's pupil (an aperture, in general) measured in mm, and  $c_2^{-2}$ ,  $c_2^0$  and  $c_2^2$  are in  $\mu\text{m}$ . Figure 4.3 illustrates a wavefront map obtained for  $S = 0.5\text{D}$ ,  $C = -2.0\text{D}$ ,  $\phi = 45^\circ$  and  $R = 1.5\text{mm}$ . If no aberration is present,

the resulting wavefront is planar.

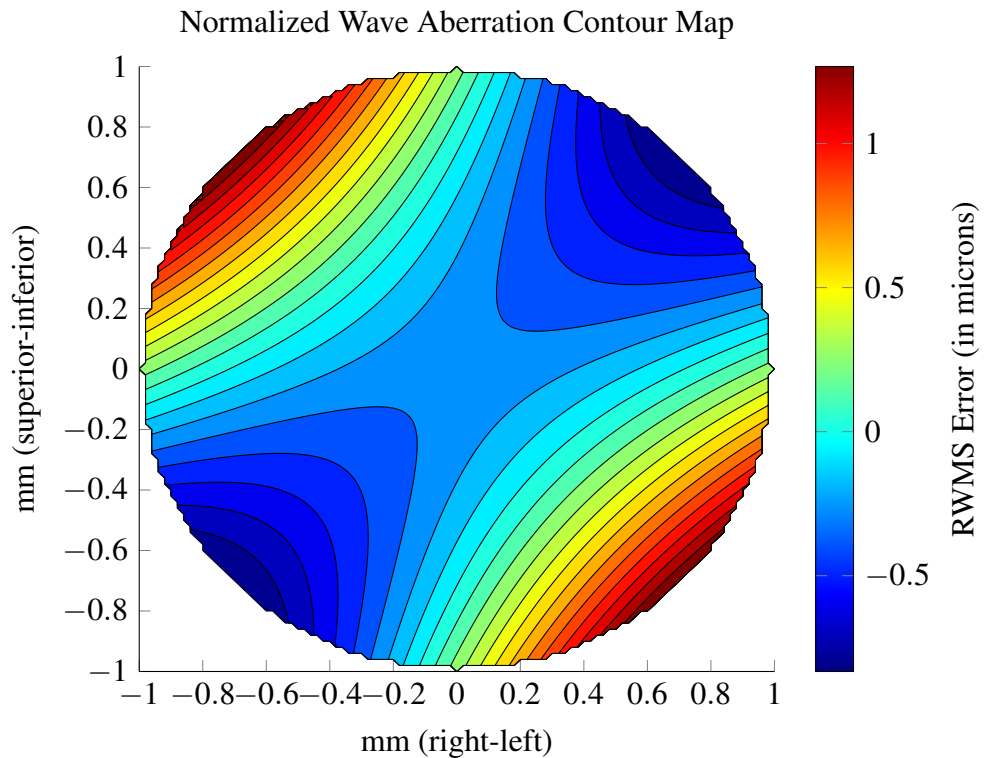


Figure 4.3 – Wavefront map for an eye with:  $S = 0.5\text{D}$ ,  $C = -2.0\text{D}$ ,  $\phi = 45^\circ$  and  $R = 1.5\text{mm}$ .

#### 4.2.1 Vertex Distance and Ray Transfer Matrix

The optical power of a lens prescribed for correcting low-order aberrations varies according to the type of lens. This happens due to the distance from the lens to the cornea, also known as *vertex distance* (Figure 4.4). While the vertex distance from the cornea to a contact lens is 0mm, its distance to an eyeglass is usually 12mm. To compensate for the spacing between pairs of optical elements, we use a *ray transfer matrix* to describe the light path through the optical system. Glytsis (2014) provides a step-by-step description of the process involved in computing a ray transfer matrix. Annex A discusses how to obtain the new focal length and magnification value for an optical system consisting of multiple lenses.

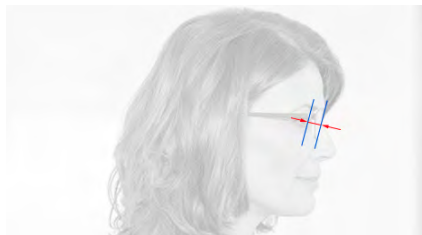


Figure 4.4 – Typical eyeglasses vertex distance of 12mm.

### 4.3 Image Filtering

Given  $S$ ,  $C$ ,  $R$ , and  $\phi$ , one can obtain the effective aberration function as  $kW_{(x,y)}$ , where  $k$  is the spherical wavenumber (*i.e.*,  $k = 2\pi/\lambda$ ), and  $W_{(x,y)}$  is the wavefront aberration function expressed using the Zernike polynomials. For the case of low-order aberrations,  $W_{(x,y)}$  is defined by Equation 4.3, which takes into account oblique astigmatism, defocus, and vertical astigmatism.  $\lambda = 550nm$  is a standard wavelength used for monochromatic simulation (DAI, 2008). The pupil function  $P_{(x,y)}$  is a binary function that evaluates to 1 inside the projected aperture, and 0 outside it. According to Goodman (2005), the *generalized pupil function*  $\mathbb{P}_{(x,y)}$  is given by:

$$\mathbb{P}_{(x,y)} = P_{(x,y)} \exp[j * k * W_{(x,y)}], \quad (4.7)$$

where  $j = \sqrt{-1}$ . Note that  $\mathbb{P}_{(x,y)}$  is a complex number. One can obtain the point spread function of the optical system as the power spectrum of  $\mathbb{P}$ , *i.e.*,  $PSF = |\mathcal{F}(\mathbb{P})|^2$ , where  $\mathcal{F}$  is the Fourier transform operator. Given the PSF and an input image  $I$ , one can simulate the view of  $I$  through the given optical system computing the 2-D convolution  $O = PSF \otimes I$ . A more efficient computation of  $O$  can be obtained in the frequency domain (this is illustrated by purple arrows in Figure 4.1). In that case,  $O = \mathcal{F}^{-1}(\mathcal{F}(I) * OTF)$ , where  $OTF = \mathcal{F}(PSF)$  is the *optical transfer function* and  $*$  is the element-wise multiplication.

### 4.4 Validation

To validate the visual simulation results of the refractive errors, we use DSLR camera (Canon model EOS Rebel T3 with 18-55mm lens). The camera represents a perfect eye (*i.e.* without refractive aberrations). We place additional lenses in front of the camera's optical system to induce low-order aberrations (*i.e.*, myopia, hyperopia, and astigmatism). Such lenses are placed on a support fixed to a UV filter attached to the main lens. Figure 4.5(a) shows the camera with an external +1.0 diopter lens attached to it. The support can hold up to three additional lenses. We have also created a synthetic eye model and adjusted it according to the camera's configuration to achieve consistent results. When comparing results, we make sure that the *f-number* (*i.e.*, the ratio of the lens' focal length  $f$  to the diameter  $D$  of the entrance pupil):

$$f_{number} = \frac{f}{D} \quad (4.8)$$

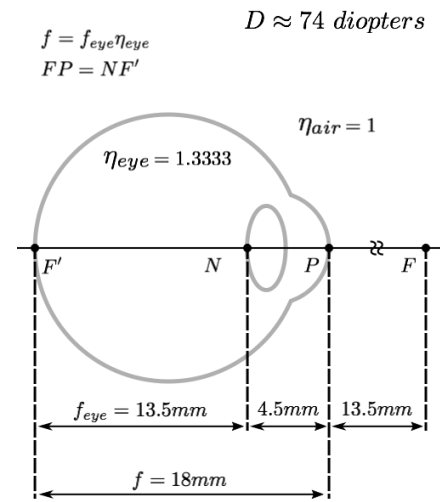
is the same for the optical systems of both the camera and the synthetic eye. For the experiments, we setup the focal length of the camera's main lens to 18mm (regardless of the use or not of additional lenses). Thus, for  $f$ -number values of 4.0, 4.5 and 5.0, the camera lens aperture would be 4.5mm, 4.0mm and 3.6mm, respectively. Our synthetic eye model (Figure 4.5(b)) has an axial diameter of 18mm. Due to the presence of the crystalline lens, its actual focal length of 13.5mm:  $f_{eye} = 18mm \times \eta_{eye} = 18mm \times 1.333 = 13.5mm$ , where  $\eta_{eye}$  is the index of refraction of the eye. As a result, for the simulations, the pupil size (equivalent of the camera's lens aperture) needs to be rescaled to maintain the same  $f$ -number values as the camera. Table 4.1 shows the corresponding values of the equivalent camera apertures and pupil diameters. The simulation results shown in Chapter 5 were obtained for  $f/5.0$ .

Table 4.1 – Camera apertures and pupil diameters for various f-numbers.

<b>f-number</b>	<b>DSLR Camera (18mm focal length)</b>	<b>Synthetic Eye (13.5mm focal length)</b>
	<b>aperture</b>	<b>pupil diameter</b>
$f/4.0$	4.5mm	3.4mm
$f/4.5$	4.0mm	3.0mm
$f/5.0$	3.6mm	2.7mm



(a)



(b)

Figure 4.5 – Optical systems used in the validation process: (a) Canon EOS Rebel T3 with apparatus to add up to three extra lenses. Focal lens set to 18mm; (b) synthetic eye model with effective focal length of 13.5mm.

#### 4.4.1 Comparison of Simulated Results with Ground Truth

The MATLAB Student Version (R2014a) environment has been chosen to implement the simulation technique described in this thesis.



This section compares our simulated results with an optical ground truth, obtained by capturing images of a vision chart containing Sloan letters produced using Equation 4.1 and placed at three feet from the camera. Figures 4.6 and 4.7 compare images of black letters against a white background captured by the DSLR camera (top row) against the results of our simulations (middle row). The images in the top row were captured by the camera with extra lenses, ranging from 0 to +4 diopters, in steps of 1 diopter. In the middle, one sees the resulting images produced using our technique.

Even though the final arbiter of image quality is the human viewer, we've adopted two objective metrics — the Structural Similarity (SSIM) Index and the Peak Signal-to-Noise Ratio (PSNR) — to measure quality. Tables 4.2 and 4.3 show the comparison results between the ones presented in Figures 4.6 and 4.7. Each row of the tables represents the value of a specific metric (*i.e.*, SSIM or PSNR) when comparing an image capture by the DSLR camera with the one simulated using our technique. The SSIM metric is a decimal value between -1 (poor similarity) and 1 (high similarity) and it is calculated for each pixel in an image, based on its

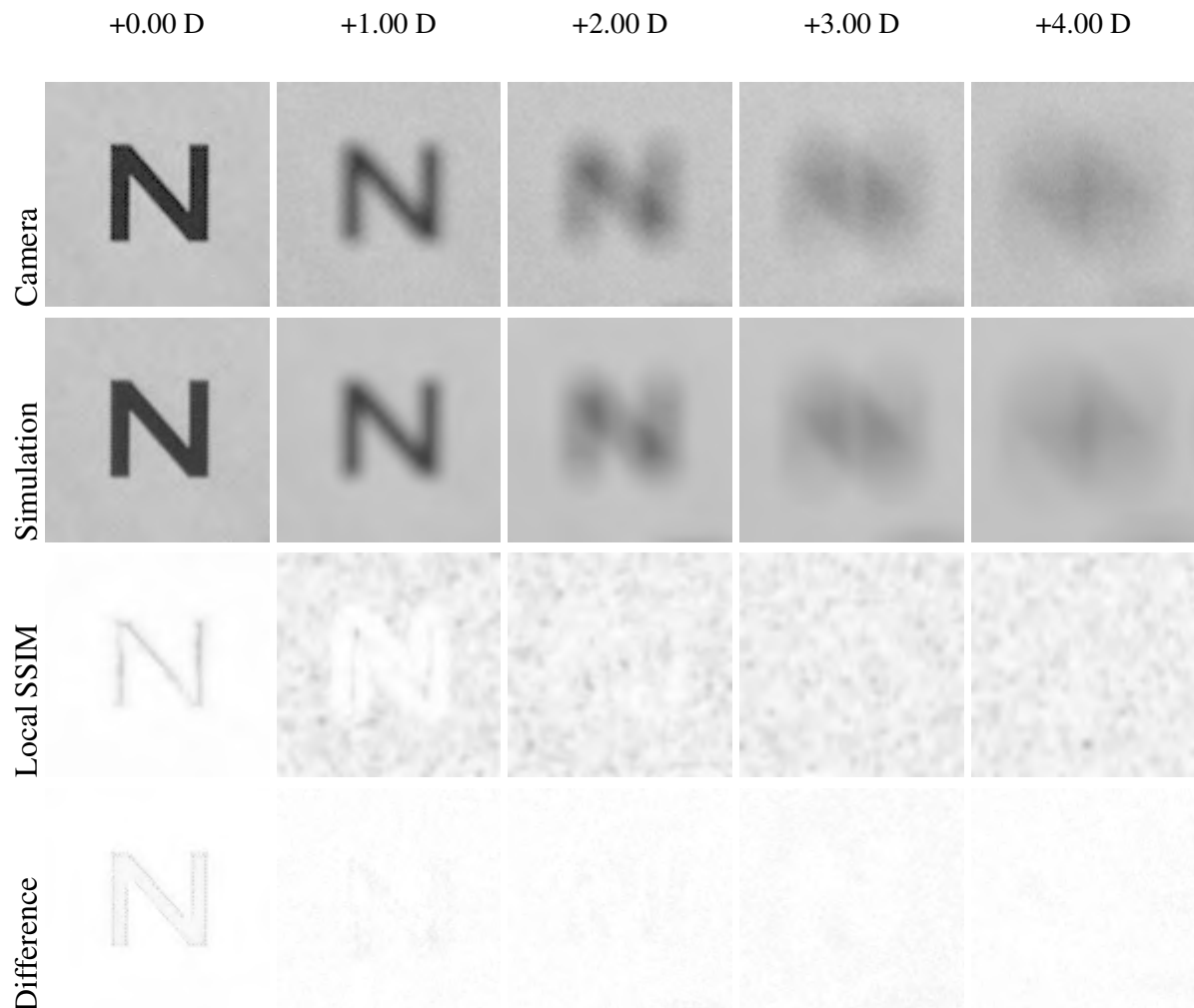


Figure 4.6 – Myopic perception of 20/200 Sloan black letters

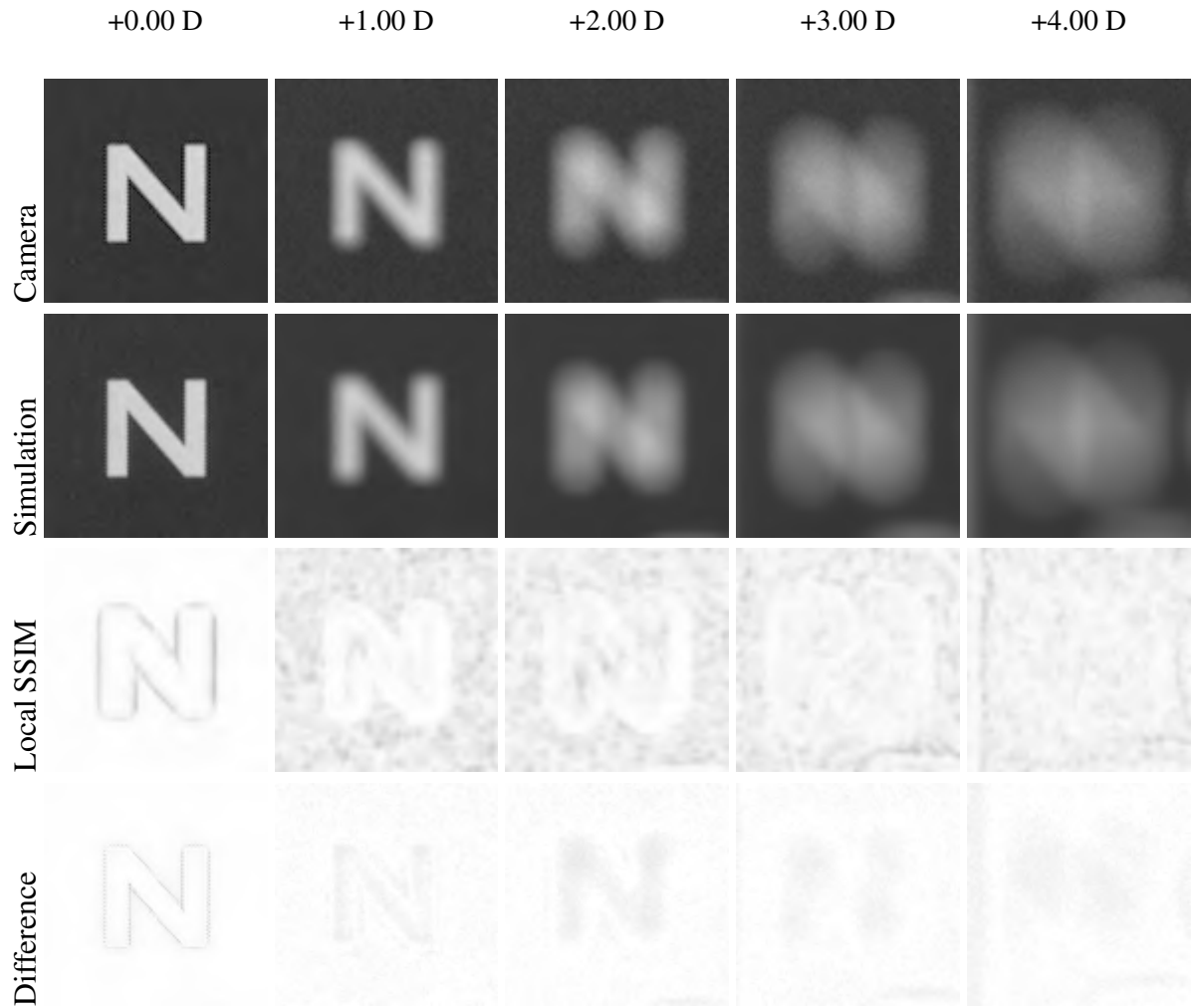


Figure 4.7 – Myopic perception of 20/20 Sloan white letters

relationship to other pixels in an 11-by-11 neighborhood. It is possible to visualize the results of this metric as an image, which represents the local (*i.e.*, pixel-by-pixel) SSIM index. Such images are illustrated in Figures 4.6(bottom row) and 4.7(bottom row). We’ve obtained the PSNR by calculating the mean squared error (MSE) and then dividing the maximum signal value that exists in our optical ground truth image by the MSE. This metric is given in decibel and relies strictly on numeric comparison between images. When two images are identical, the

Table 4.2 – SSIM and PSNR table of myopic perception (Figure 4.6)

	<b>+0.00 D</b>	<b>+1.00 D</b>	<b>+2.00 D</b>	<b>+3.00 D</b>	<b>+4.00 D</b>
<b>SSIM</b>	0.9834	0.9384	0.9428	0.9484	0.9490
<b>PSNR</b>	34.6491	35.7883	33.8015	35.2325	33.2118

Table 4.3 – SSIM and PSNR table of myopic perception (Figure 4.7)

	<b>+0.00 D</b>	<b>+1.00 D</b>	<b>+2.00 D</b>	<b>+3.00 D</b>	<b>+4.00 D</b>
<b>SSIM</b>	0.9869	0.9378	0.9324	0.9296	0.9322
<b>PSNR</b>	34.7779	38.8748	38.7219	35.6993	39.3720

PSNR tends to infinity. Excellent values range from 30 to 50 dB, where higher is better.

Similarly, Figures 4.8 and 4.9 show examples of a hyperopic perception of Sloan letters. The results in the top row were produced, as in the previous setup, by using a DSLR camera and extra lenses, ranging from 0 to -4 diopters, in steps of -1 diopter. In Figures' simulation row, one sees the resulting images produced using our technique. The comparison results between the images are shown in Tables 4.4 and 4.5. The bottom row presents the visualization of the pixel-by-pixel SSIM index when comparing the hyperopic results. ~~The main diagonal contains the fundamental comparisons, that is, the comparisons between the images captured with a specific additional asdasdasda sdasdasd asdasdasdasd asdasdasd.~~

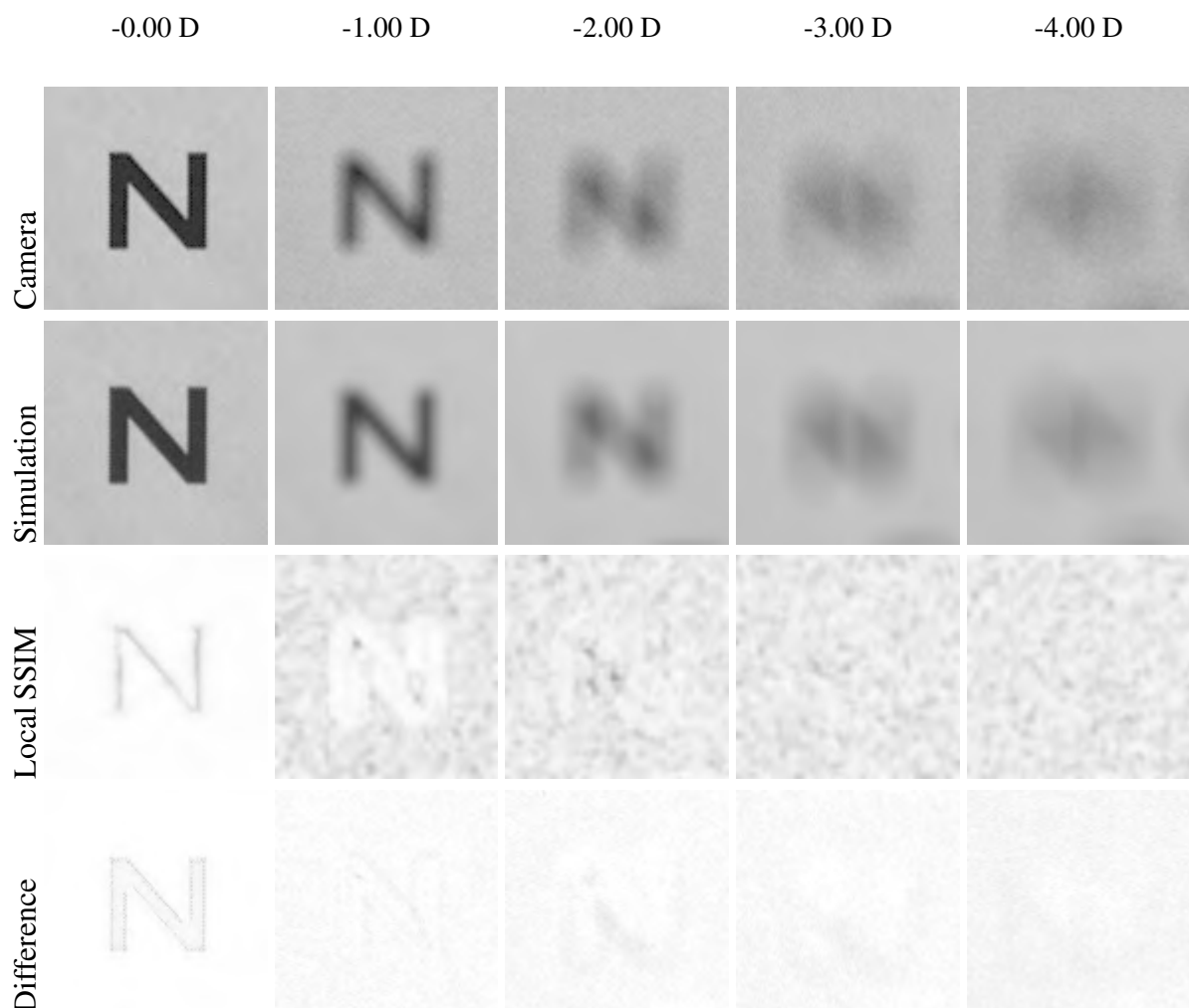


Figure 4.8 – Hyperopic perception of 20/200 Sloan black letters

We've also explored simulations of more effects rather than defocus. Figures 4.10 and

Table 4.4 – SSIM and PSNR table of hyperopic perception (Figure 4.8)

	-0.00 D	-1.00 D	-2.00 D	-3.00 D	-4.00 D
SSIM	0.9869	0.9192	0.9149	0.9119	0.9130
PSNR	34.7778	34.3781	32.8601	32.6680	29.5003

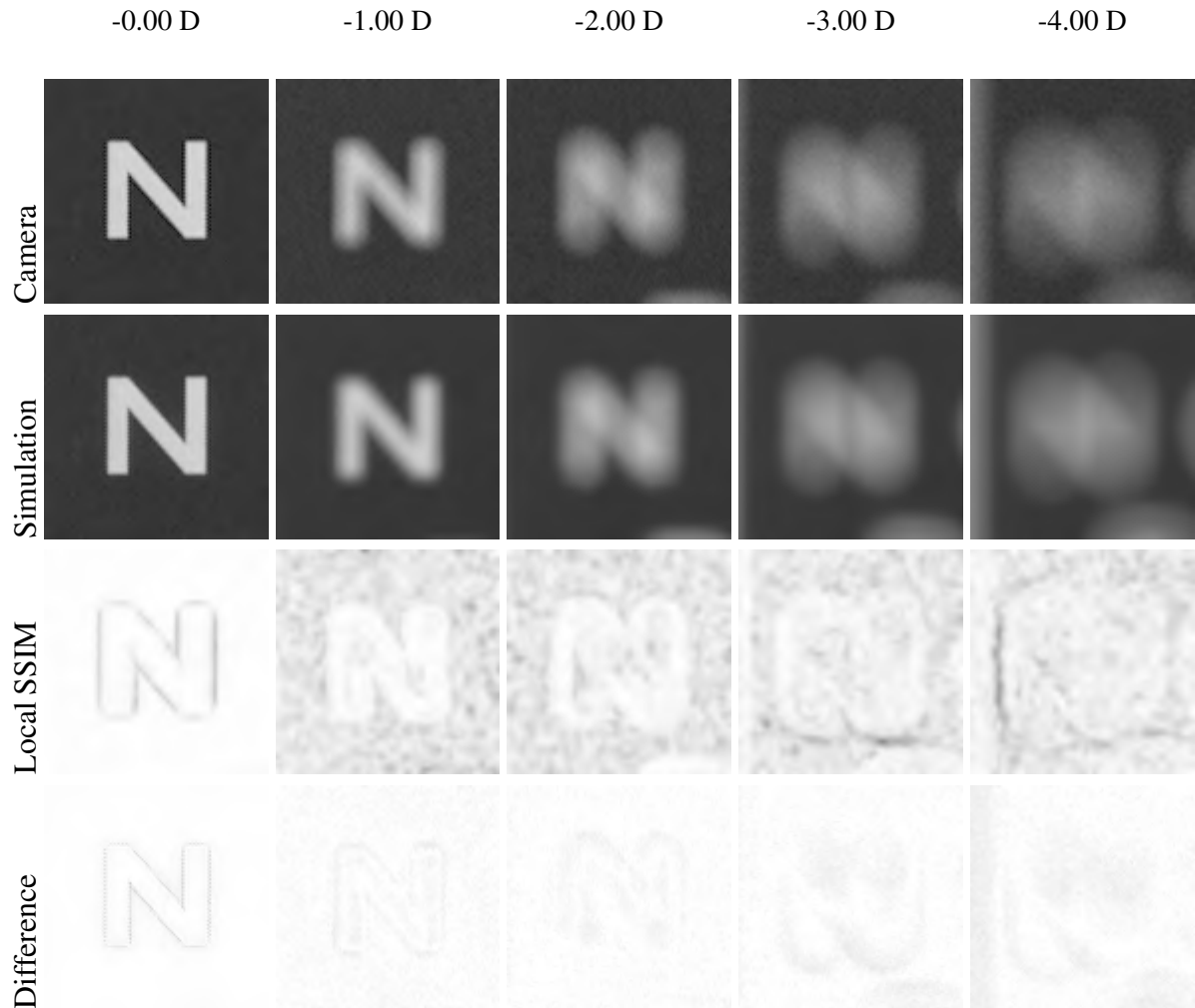


Figure 4.9 – Hyperopic perception of 20/200 Sloan white letters

4.11 shows the simulation of an astigmatic perception. The Sloan letters in Figures 4.10 were captured by the DSLR camera with an additional negative-cylindrical lens with 2 diopters, rotated in order to simulate astigmatism in the horizontal meridian. Similarly, Figure 4.11 shows the real and simulated astigmatism in the vertical meridian. In the same way, we've used a positive-cylindrical lens with 2 diopters to simulate an astigmatic perception of white Sloan letters (Figures 4.12 and 4.13). Both astigmatic simulations outcomes were evaluated using the SSIM and PSNR metrics, and the resultant values when comparing the simulated images to the reference ones are shown in Tables 4.6 and 4.6.

Note that part of the disparities present in some of the astigmatic local SSIM index visualizations (comparison images of Figures 4.10, 4.11, 4.12 and 4.13) may be caused due to

Table 4.5 – SSIM and PSNR table of hyperopic perception (Figure 4.9)

	-0.00 D	-1.00 D	-2.00 D	-3.00 D	-4.00 D
<b>SSIM</b>	0.9833	0.9157	0.9196	0.9213	0.9165
<b>PSNR</b>	34.6438	35.0465	36.6722	33.3992	30.9853

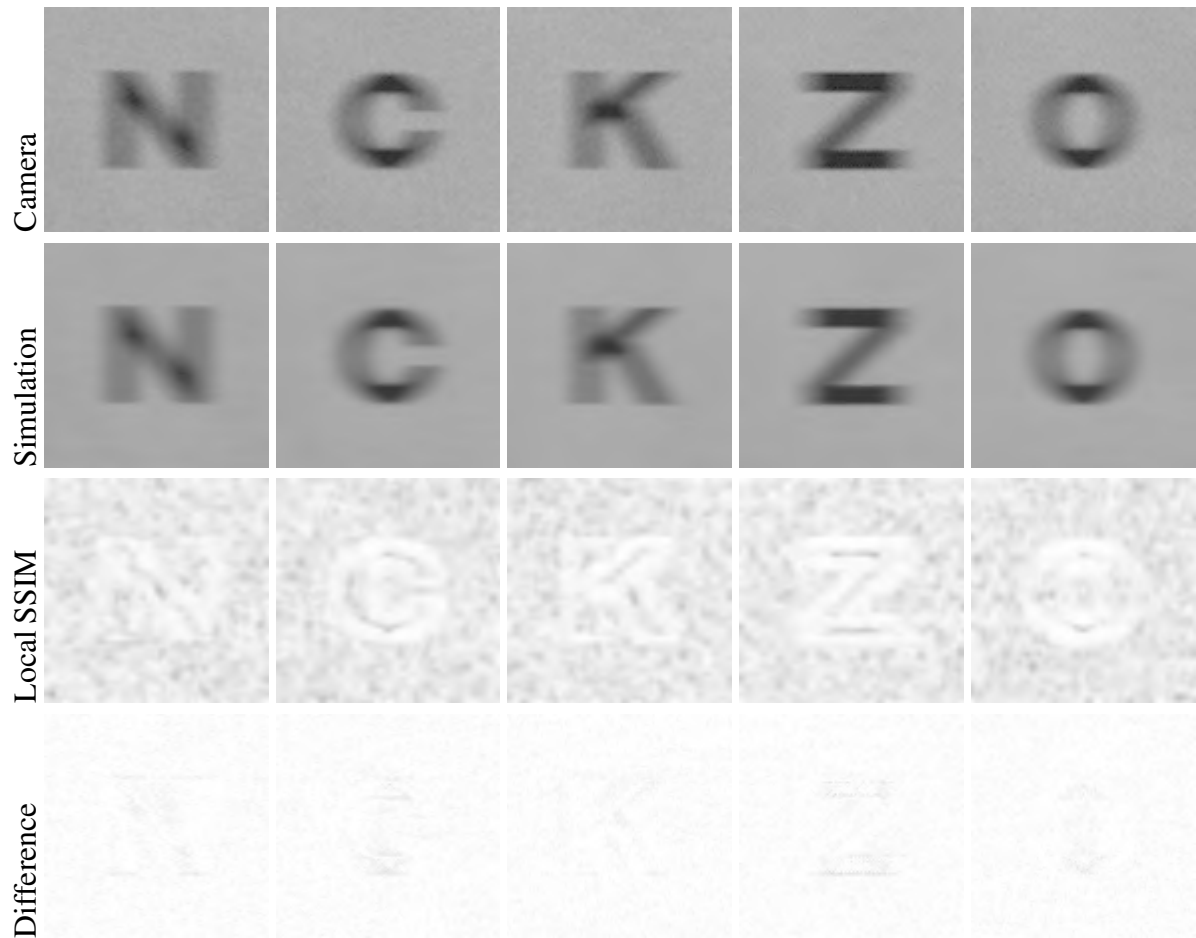


Figure 4.10 – Astigmatic perception of 20/200 Sloan black letters (-2 @90)

the imperfect lens positioning. As we need to precisely align the astigmatic axis to the ones configured in our simulations, any displacement interferes in the final quality.

~~colocar algum texto aqui para que o alinhamento das imagens fique como está. colocar algum texto aqui para que o alinhamento das imagens fique como está. colocar algum texto aqui para que o alinhamento das imagens fique como está. colocar algum texto aqui para que o alinhamento das imagens fique como está. colocar algum texto aqui para que o alinhamento das imagens fique como está. colocar algum texto aqui para que o alinhamento das imagens fique como está. colocar algum texto aqui para que o alinhamento das imagens fique como está.~~

Figures 4.14 and 4.15 show the simulation of myopia when looking to several 20/200 Sloan letters with different background colors at a distance of three feet. The input column of both figures present the synthetic Sloan letters used as reference to perform the simulations

Table 4.6 – SSIM and PSNR table of the negative astigmatic perception.

		N	C	K	Z	O
<b>-2.00 @90</b>	<b>SSIM</b>	0.9171	0.9174	0.9193	0.9242	0.9185
	<b>PSNR</b>	36.4269	36.0369	37.0615	35.9831	36.9738
<b>-2.00 @180</b>	<b>SSIM</b>	0.9169	0.9207	0.9226	0.9220	0.9201
	<b>PSNR</b>	34.6329	37.8456	37.4705	38.7289	37.8041

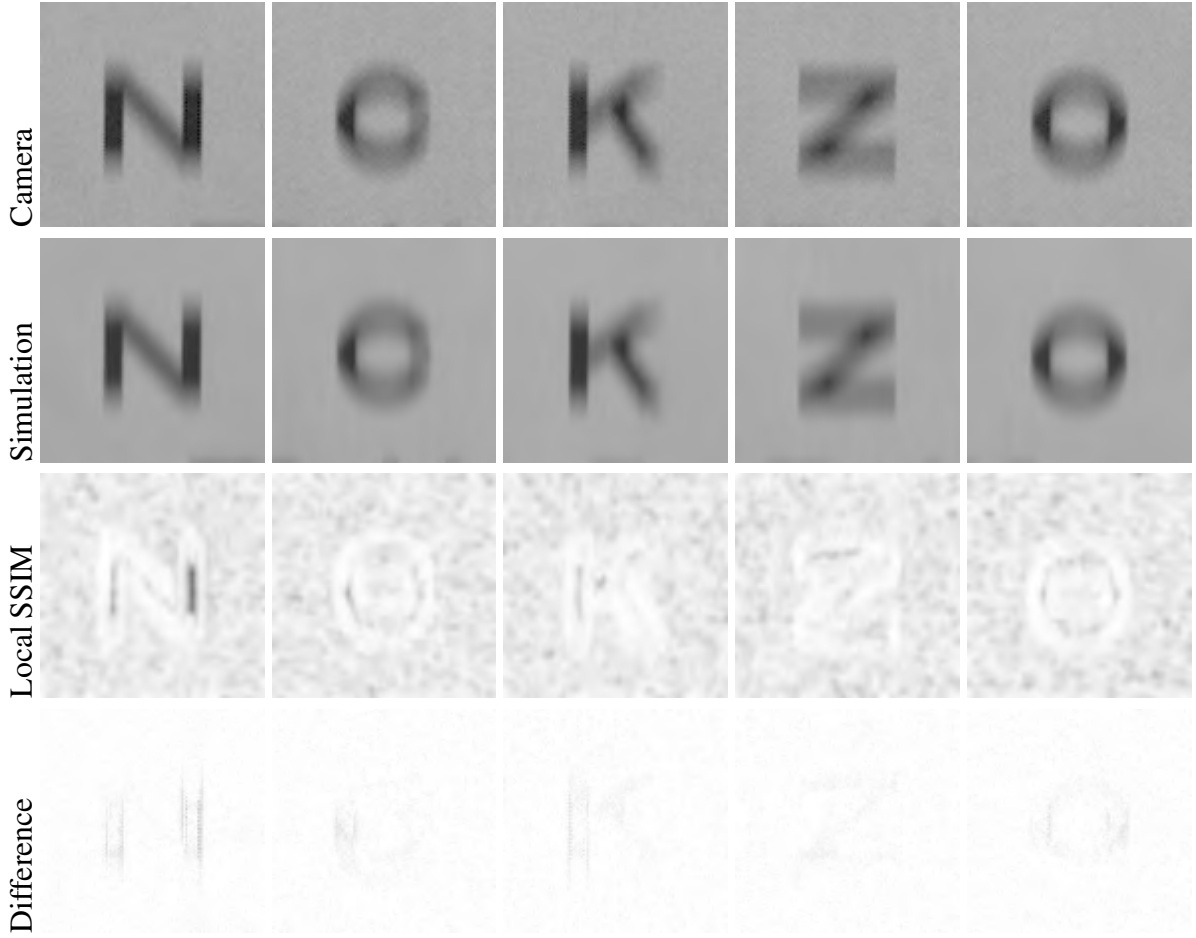


Figure 4.11 – Astigmatic perception of 20/200 Sloan black letters (-2 @180)

illustrated in the following column. The others columns are related to the optical ground truth comparison, with the use of additional lenses and a DSLR camera. Note that as our method involves the convolution of the image with a blurring kernel (*i.e.*, PSF), the noise of the reference optical images (camera ones) is attenuated in our simulations (simulation ones).

Our method can also be used to simulate any combination of visual aberrations. Even though its validation depends on the existence of an optical ground truth, the method is not limited to the ones configured in previous camera's setup. Figure 4.16 (top row) shows how a combination of low-order aberrations (myopia and astigmatism) affect the perception of a Sloan letter. Figures 4.16(b) and 4.16(c) illustrate the intermediate steps involved in the blurring process, representing the normalized aberrated wavefront and the spatial PSF, respectively.

Table 4.7 – SSIM and PSNR table of the positive astigmatic perception

		N	C	K	Z	O
<b>+2.00 @90</b>	<b>SSIM</b>	0.9307	0.9271	0.9277	0.9193	0.9303
	<b>PSNR</b>	37.2835	35.4130	36.3713	32.7150	36.2564
<b>+2.00 @180</b>	<b>SSIM</b>	0.9235	0.9287	0.9257	0.9308	0.9260
	<b>PSNR</b>	33.3036	36.8478	35.0677	36.5272	36.2953

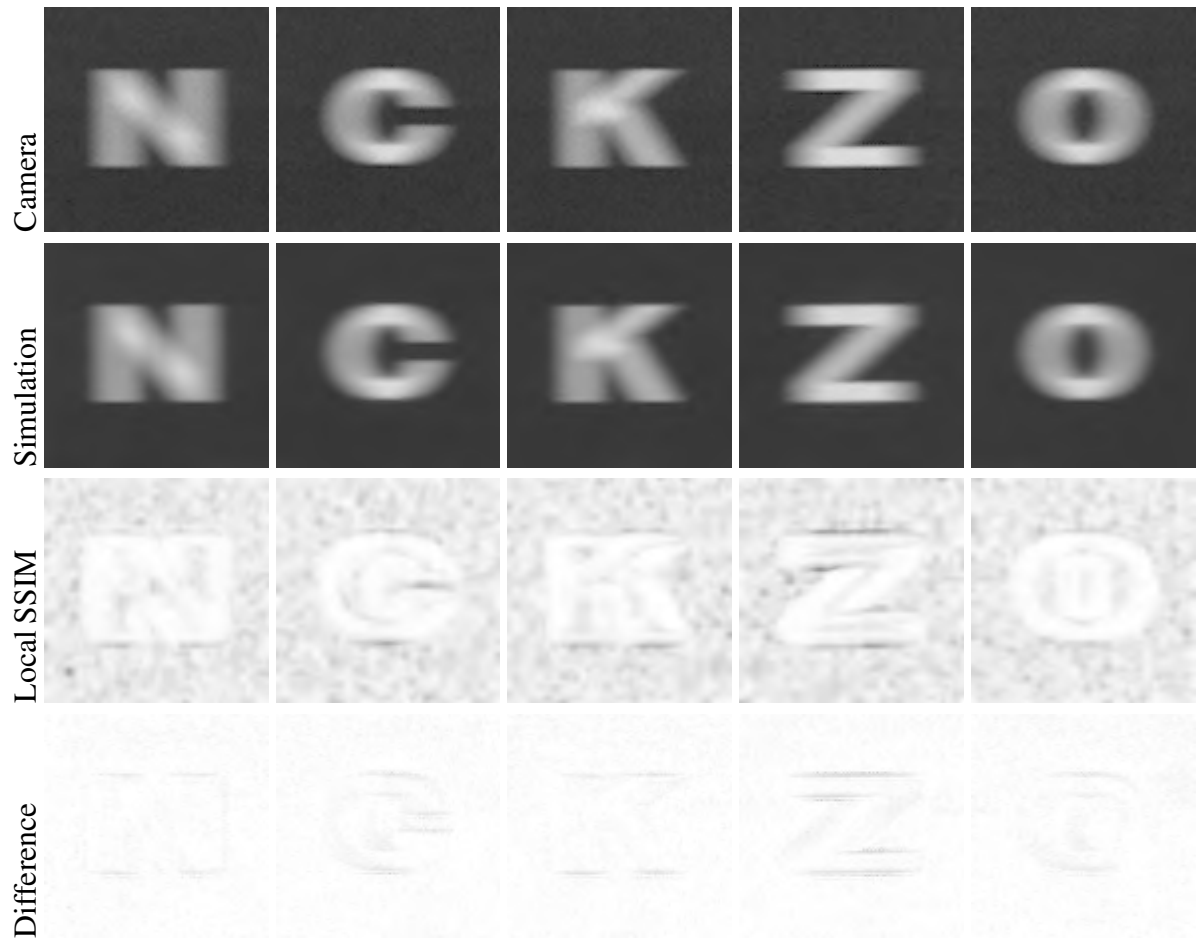


Figure 4.12 – Astigmatic perception of 20/200 Sloan white letters (+2 @90)

Figures 4.16 (e-l) simulates higher values of pure astigmatism or spherical aberration than the ones possible to capture with our trial lens set. Finally, Figure 4.16 (bottom row) shows the simulation outcomes when considering only higher-order aberrations. For these results, we've generated arbitrary values for some of the wavefront's coefficients ( $j = 6$ ,  $j = 7$ ,  $j = 9$ ,  $j = 13$ ,  $j = 15$  and  $j = 18$ ) described in Section 2.3.2.

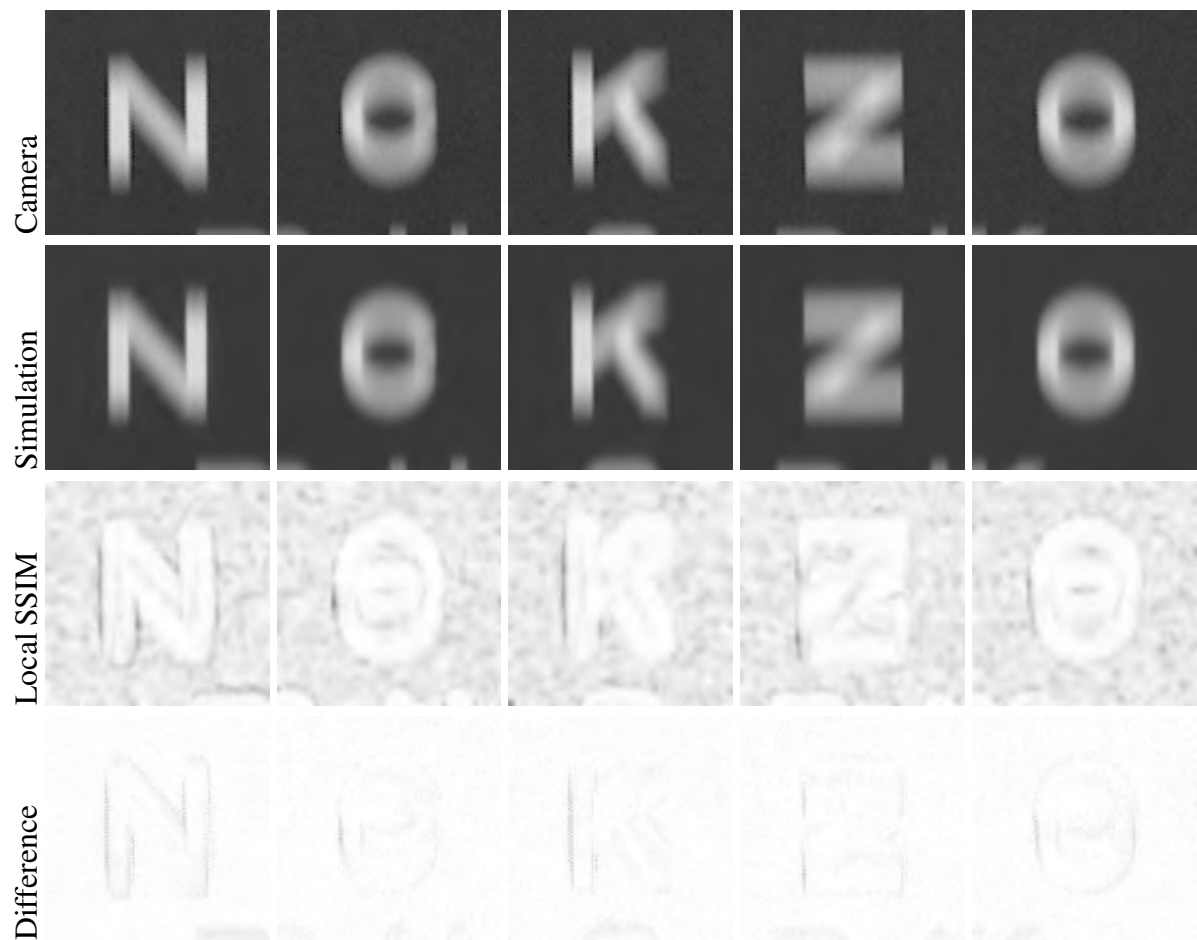


Figure 4.13 – Astigmatic perception of 20/200 Sloan black letters (+2 @180)



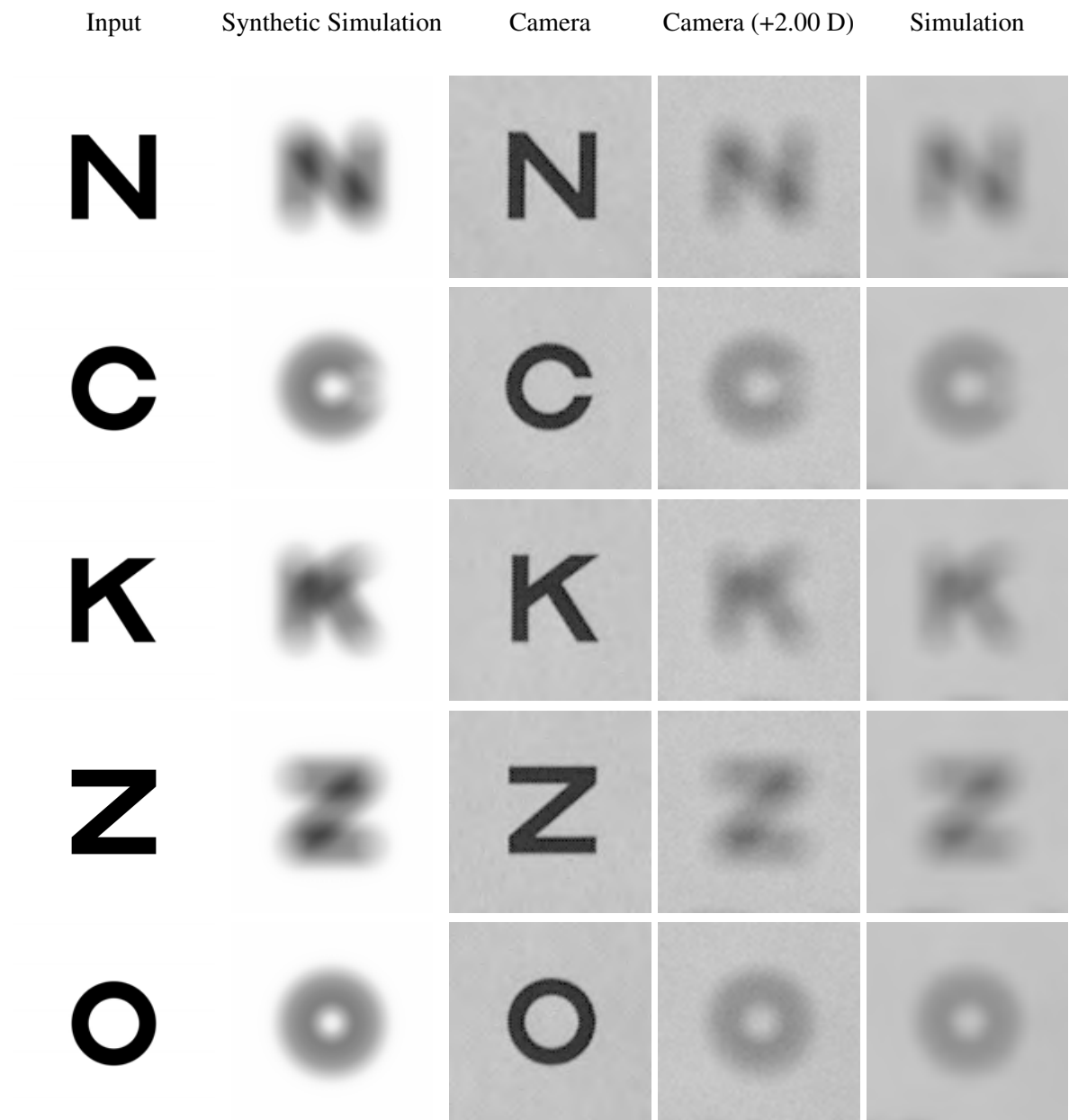


Figure 4.14 – WB, NCKZO, 20/200, +2

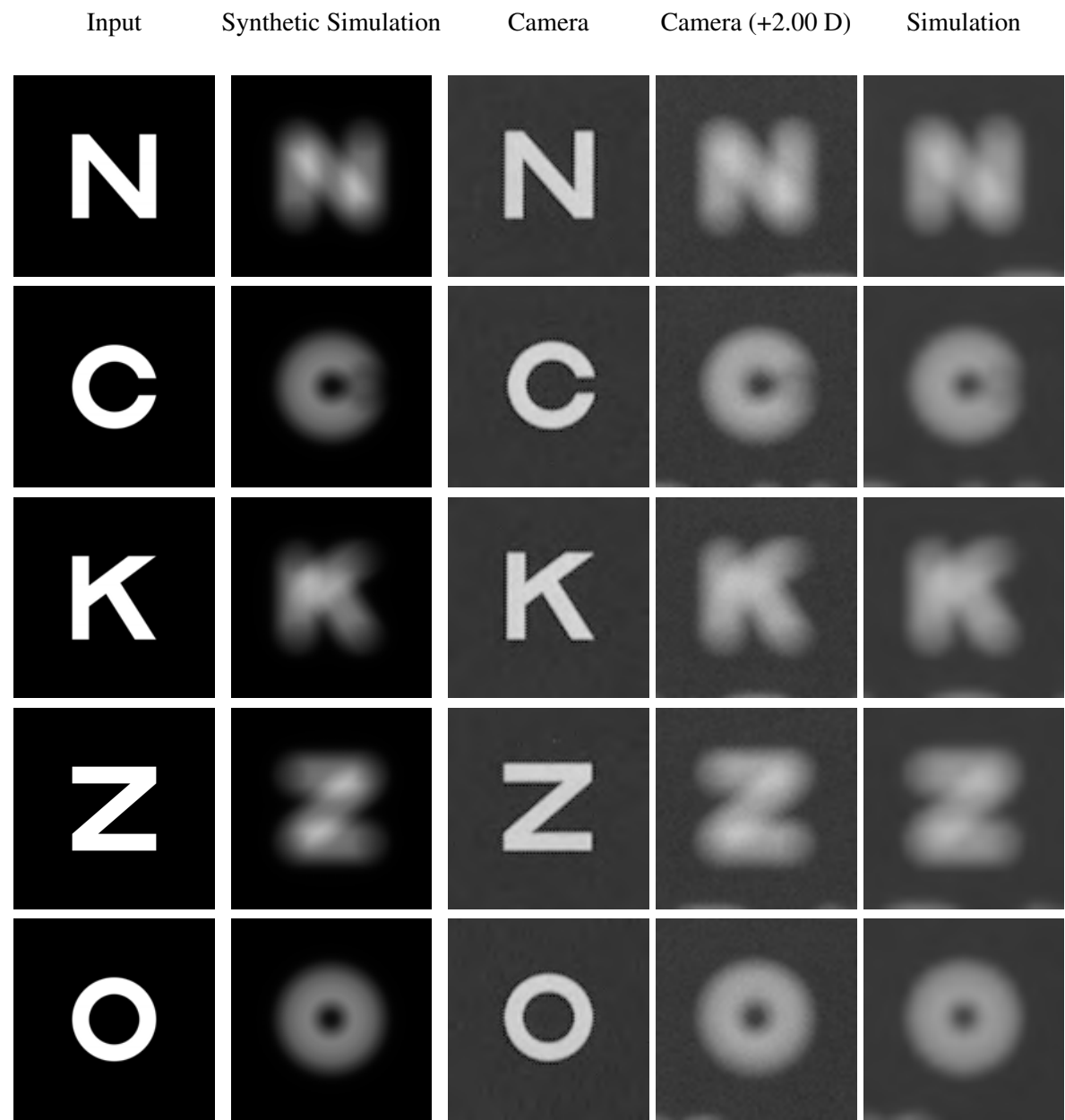


Figure 4.15 – BW, NCKZO, 20/200, +2

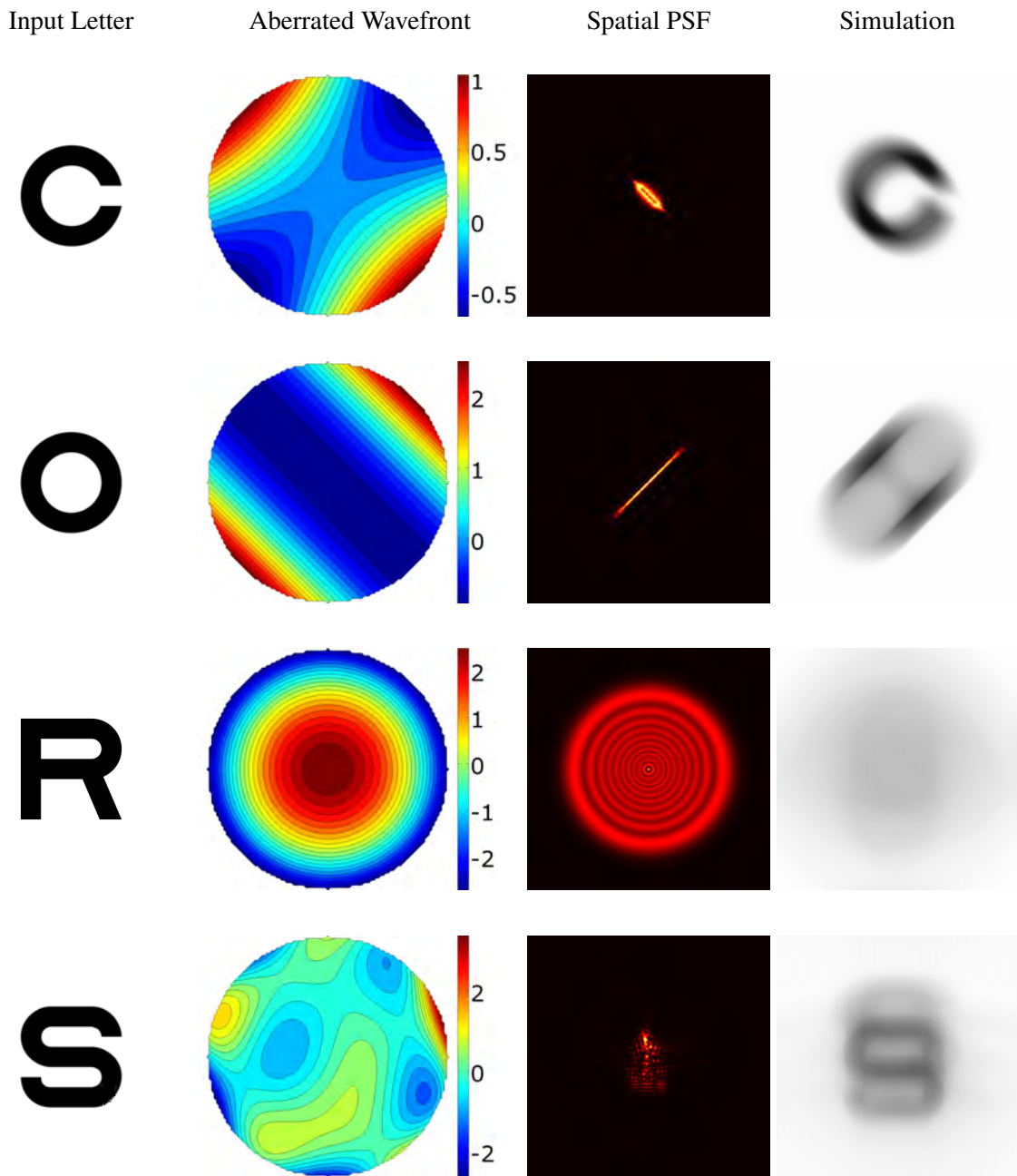


Figure 4.16 – Simulation of how lower and higher order visual aberrations affect the perception. (a) Sloan C letter, V.A. of 20/200; (b) normalized wavefront with low-order aberrations — +0.5 Sph. -2.0 Cyl. at 45; (c) spatial PSF; (d) final image after the convolution between images (a) and (c); (e) Sloan O letter, V.A. of 20/200; (f) normalized wavefront with low-order aberrations — -4.7 Cyl. at 135; (g) spatial PSF; (h) final image after the convolution between images (e) and (g); (i) Sloan R letter, V.A. of 20/200; (j) normalized wavefront with low-order aberrations — +6 Sph; (k) spatial PSF; (l) final image after the convolution between images (i) and (k); (m) Sloan S letter, V.A. of 20/200; (n) normalized wavefront with high-order aberrations —  $Z_{c=6} = 0.2$ ,  $Z_{c=7} = 0.2$ ,  $Z_{c=9} = 0.1$ ,  $Z_{c=13} = 0.2$ ,  $Z_{c=15} = 0.4$  and  $Z_{c=18} = 0.3$ ; (o) spatial PSF; and (p) final image after the convolution between images (m) and (o).



## 5 ABSOLUTE THRESHOLD

We've used Objective-C to implement the software adopted in the absolute threshold psychophysical experiment. In this chapter, we present many examples using extra lenses to simulate low-order aberrations. We also show that, by using our technique, we can achieve similar results if comparing with real ones. Finally, we present the results of the psychophysical experiment.

### 5.1 Absolute Threshold

Besides the previously discussion about optical aberrations that affect visual perception, there are non-optical characteristics (*i.e.*, intrinsic phenomena to an individual) which can be considered in the simulation to achieve more realistic rendering of retinal images. In this section, we discuss an attempt to relate an individual's intrinsic characteristic — the absolute threshold (also known as the minimum visible) with optical aberrations values. Also, we try to integrate it in the optical simulation pipeline. When a focal imaging system (*e.g.*, human eye) is mis-focused on a point in the scene, the light emitted/reflected by it is spread out across some area of retinal surface, causing blur (a geometrical perspective of this blur is presented in Figure 5.1). Since our eye's photoreceptors have a threshold to produce a neural signal that indicates the presence of light, the bigger the blur, the bigger the must be the intensity to trigger a neural signal of the perception of light.

By considering this statements, we've created the following hypothesis:

$H_0$ : the absolute threshold does not relates directly with the eye's spherical aberration.

$H_1$ : the absolute threshold relates directly with the eye's spherical aberration.

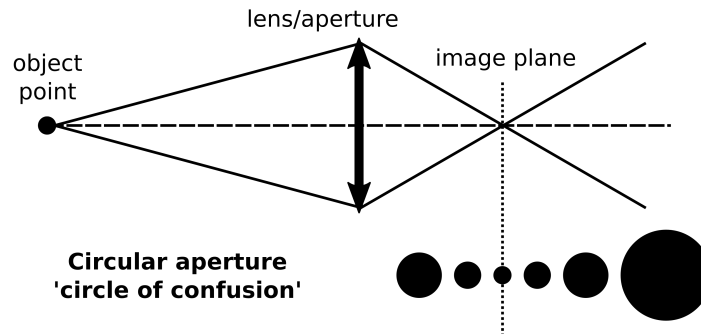


Figure 5.1 – Geometrical perspective of the circle of confusion

In the following subsections we discuss the psychophysical experiment established to

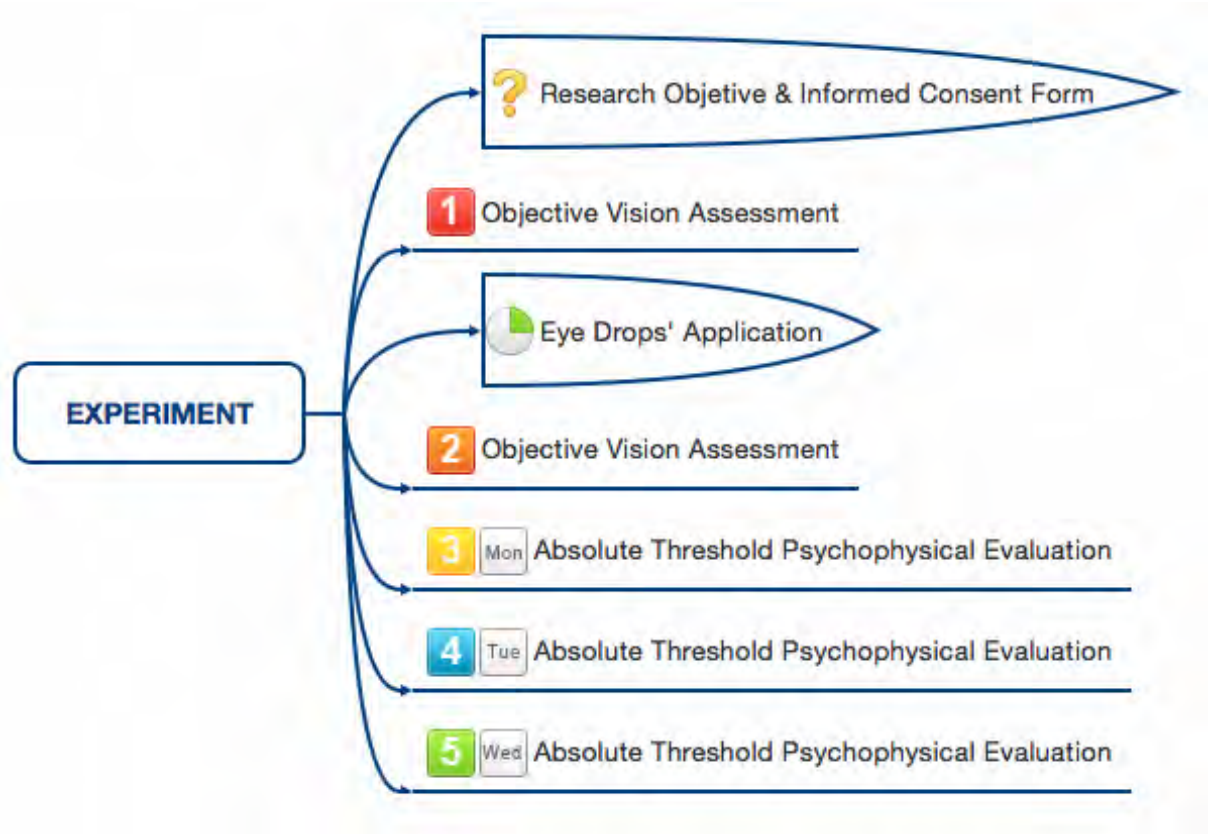


Figure 5.2 – Absolute Threshold Experiment stages

capture absolute threshold information. The population sample is presented together with the quasi-random algorithm used during the experiments. Finally, we detail a simple way for generating retinal images deeming this specific non-optical aberration.

### 5.1.1 Experimental Design

In order to find the correlation between the absolute threshold and spherical aberration (*i.e.*, validate  $H_1$  and refute  $H_0$ ), we've prepared a controlled experiment (Figure 5.2). First of all, participants were informed about the risks, burdens and benefits of the research. Next, individuals were invited to assess their vision by using a standard ophthalmic instrument — auto refractor (model KR-8900, from TOPCON). Following, a single drop of a cycloplegic eye drops were applied and the objective vision assessment were repeated. Then each one has performed three psychophysical experiments to establish their absolute threshold when dealing with light stimuli. It is important to note that the first psychophysical evaluation was applied in sequence with the second vision assessment. The others respected an interval of at least a day.

To achieve a statistically reliable number we have added extra lenses into the psy-

chophysical experiment. By doing this, for each participant, we could simulate 16 extra aberrations. Avoiding accommodation process was target by randomizing the extra lenses order. This order, as well as other information, are described in Appendix A.

### 5.1.2 Participants

The inclusion criteria for the study stipulates that all participants must be able to perform subjective, objective and auto-refraction. In total, 23 individuals meeting the inclusion criteria were asked to to participate. Three were excluded from the study due to their availability restrictions.

### 5.1.3 Quasi-Random Algorithm

The algorithm developed to determine the absolute threshold is divided into two major steps. In the first, the objective is to limit the intensity range as minimum and fast as possible. The adopted approach guarantees that, in the best case, a single interaction is sufficient to discover the unknown range. Secondly, the user interact with the device in order to precisely determine his/her absolute threshold. The last step can be replaced by a binary search.

[verificar para usar pacote algorithm](#)

Listing 5.1 – For educational purposes

```

1 set minimum intensity to zero
2 set maximum intensity to one
3 % part 1, discovering absolute threshold range [?, ?]
4 do {
5     get a random intensity value inside [min, max], in steps of 0.1
6     turn on a single pixel in the device s screen
7     asks if the user see the stimulus with the random intensity
8
9     if stimulus is visiblex
10         maximum intensity = random intensity
11     else
12         minimum intensity = random intensity
13
14 } while (difference between maximum and minimum intensity is not 0.1)

```

```

15 % part 2, absolute threshold determination
16 < user interaction >

```

### 5.1.4 Simulation

colocar algo aqui? ou simplesmente remover?

## 5.2 Absolute Threshold

In order to capture the absolute threshold of individuals, we've designed an auxiliary apparatus to isolate external light and place lens. Many trial versions of it are illustrated in Figure 5.3(a), while the final one, built in a 3-D printer, is shown in Figure 5.3(b). We've also used an iPhone 5 to generate light stimulus and control its intensity. The distance between the plano-convex lens (8 diopters) and the mobile device's screen was set to 12.5 cm, aiming parallel rays when looking at the screen. Further, the eyecup was adapted from the viewfinder of the DSLR camera used in the optical experiments. Figure 5.4(a) shows the interior of the apparatus, which has two other distances besides the focal length (12.5 cm). But just the middle one (*i.e.*, the focal length) was explored during the experiments. We've used a digital light meter at a specific distance (3 cm) and a batch program to get the response curve and relate stimulus values with lux values. Figure 5.4 illustrate the adaptation made to isolate external light and maintain the correct distance, the light meter, and the wood device used at the lab. This analysis allowed us to generate a surface relating lux values with the stimulus' size and intensity.

Medical data from 20 individuals were captured with specialized ophthalmic equipment from a partner clinic. This data is fully described in Appendix ??, together with the results of all absolute threshold psychophysical evaluations. We've realized absolute threshold experiments as described in 5.1.1, and selected two groups of them to present partial results — from individual 1 (hyperopic) and 11 (myopic). Figure 5.5 presents a plot for each individual that combines the result of four psychophysical experiments. The blue lines represent the minimum amount of light perceived by the individuals when varying additional lenses from -5 to +5 diopters. It also consider the use of eyedrops. The red ones are the mean of three psychophysical experiments without using eyedrops (*i.e.*, crystalline lens can and will accommodate if necessary). The dashed lines stands for the data of the right eye, and the circles indicate the minimum intensity value considering all lenses. At last, the black lines indicate the individual's spherical



equivalent refraction.

To better understand the accommodation effects in the absolute threshold determination, we've elaborated a controlled experiment performed by a single individual. We've applied extra drops (3 drops in total) of the cycloplegic eye drop, and evaluated the minimum perceived intensity along time. The results of this experiment are illustrated in Figure 5.6. Figure 5.6(a) shows the apparent effect — mydriasis (*i.e.*, the dilation of the pupil). Due to the high dosage of eyedrops, such effect lasted for 10 days. However, as can be seen in Figure 5.6(b), higher dosages and short time (red line) values almost correspond to the aberration captured by the gold standard ophthalmic equipment.

Considering that absolute threshold values tends to increase according to the lens power, and we've used the least squares fitting techniques to obtain a 2nd order polynomial representation of the individuals absolute threshold. By calculating the correlation-coefficient matrix and evaluate the fit parameters, we can plot and calculate confidence intervals for a predicted response. Such internals (*i.e.*, confidence bounds) are illustrated in red-dashed lines in Figures 5.7 and 5.8. The green lines are the absolute threshold values defined by the psychophysical evaluations using eyedrops (Figures 5.7(a) and 5.8(a)) or not (Figures 5.7(b) and 5.8(a)). The fitted curve is in blue, and its lower value it is represented by a blue circle.

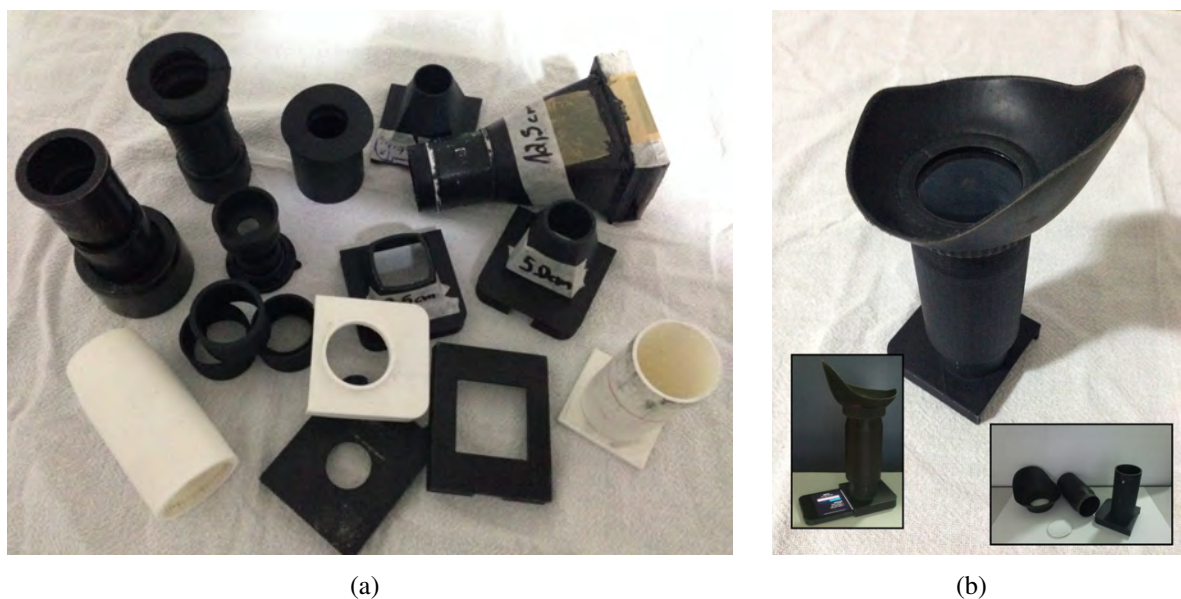


Figure 5.3 – Apparatus designed to help in the absolute threshold psychophysical evaluations

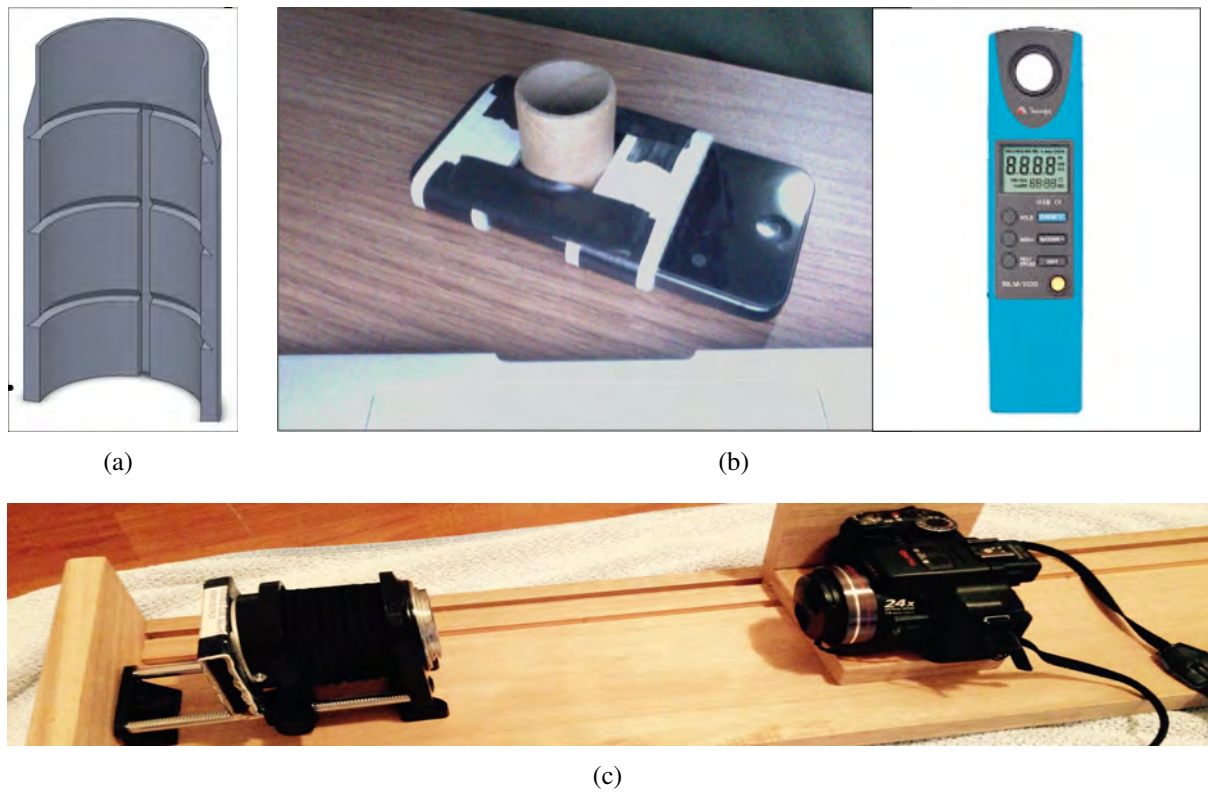


Figure 5.4 – Variations of the apparatus. (a) the interior of the final version; (b) a variant of it designed for the calibration curve acquisition process; and (c) wood device to control camera's distance.

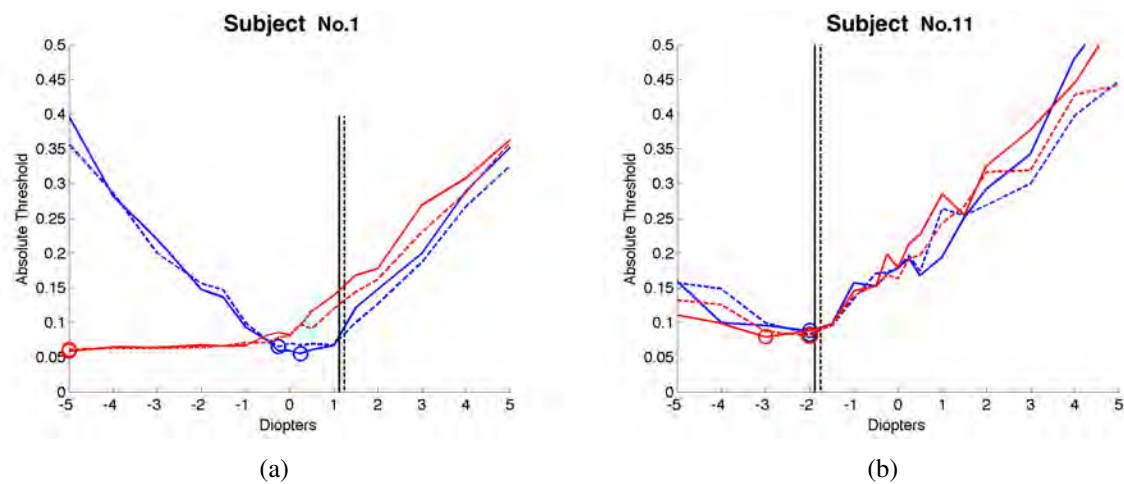
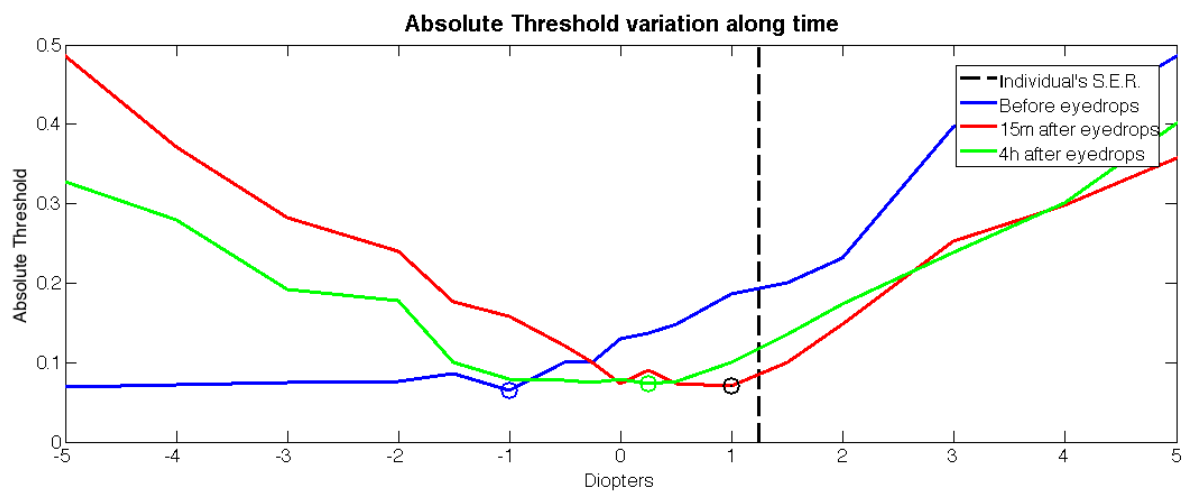


Figure 5.5 – Plot of absolute threshold data acquired with and without eyedrops. (a) a hyperopic individual from the sample; (b) a myopic individual from the sample.



(a)



(b)

Figure 5.6 – Accommodation analysis. (a) a photo of an eye with the cycloplegic eye drops' effects; (b) plot of some absolute threshold evaluations before and after the use of eye drops.

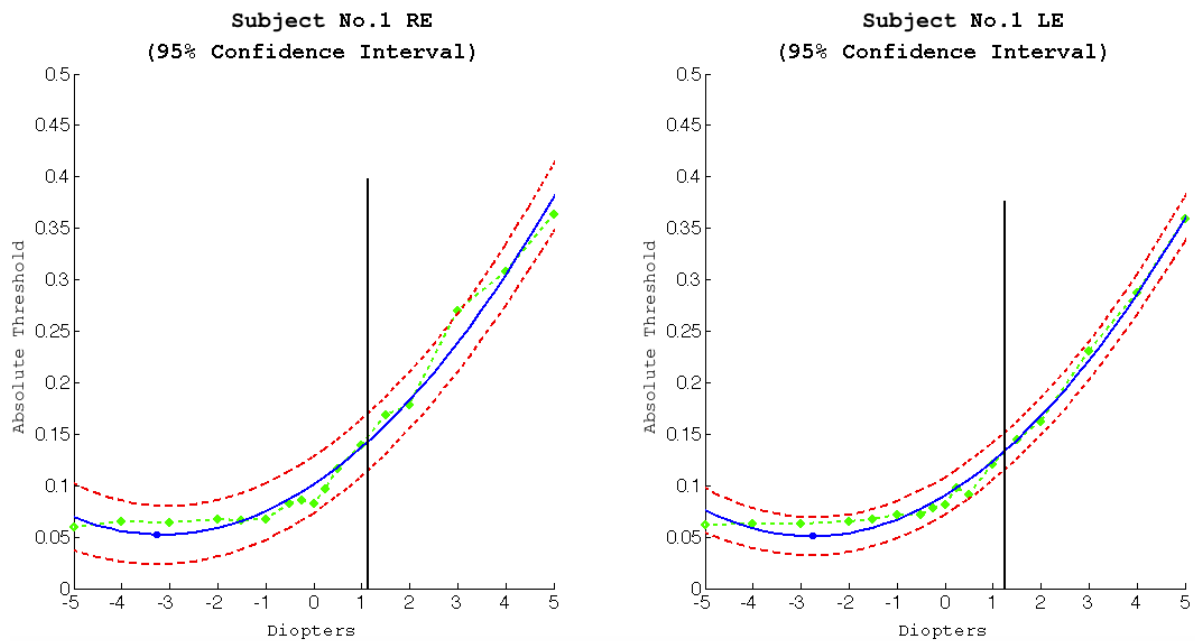
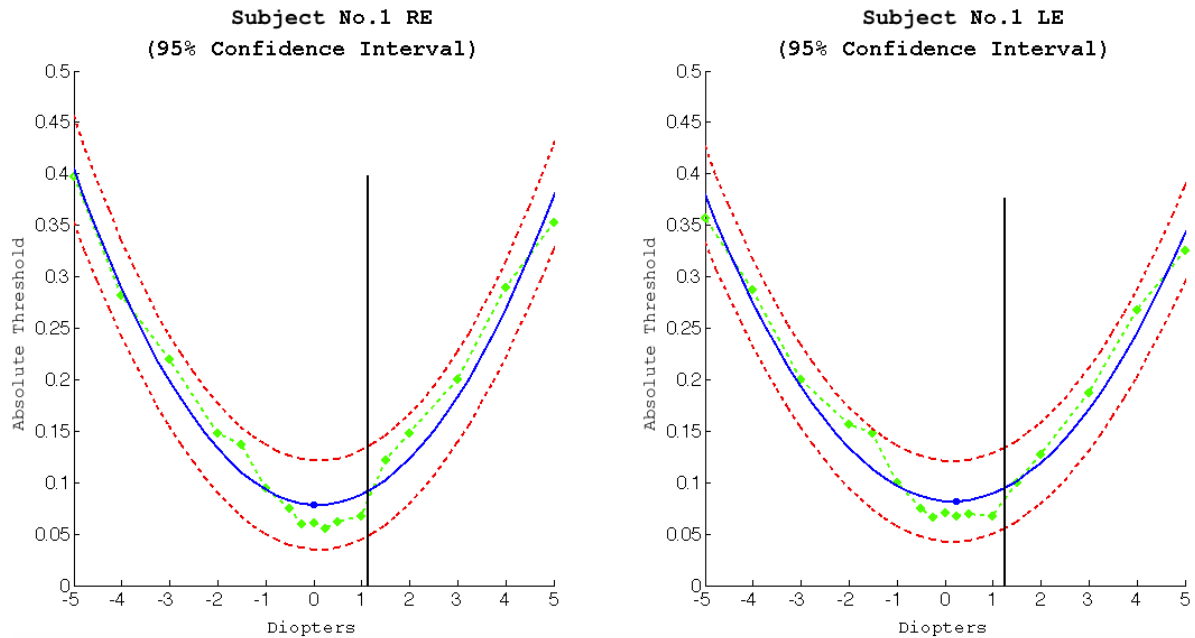
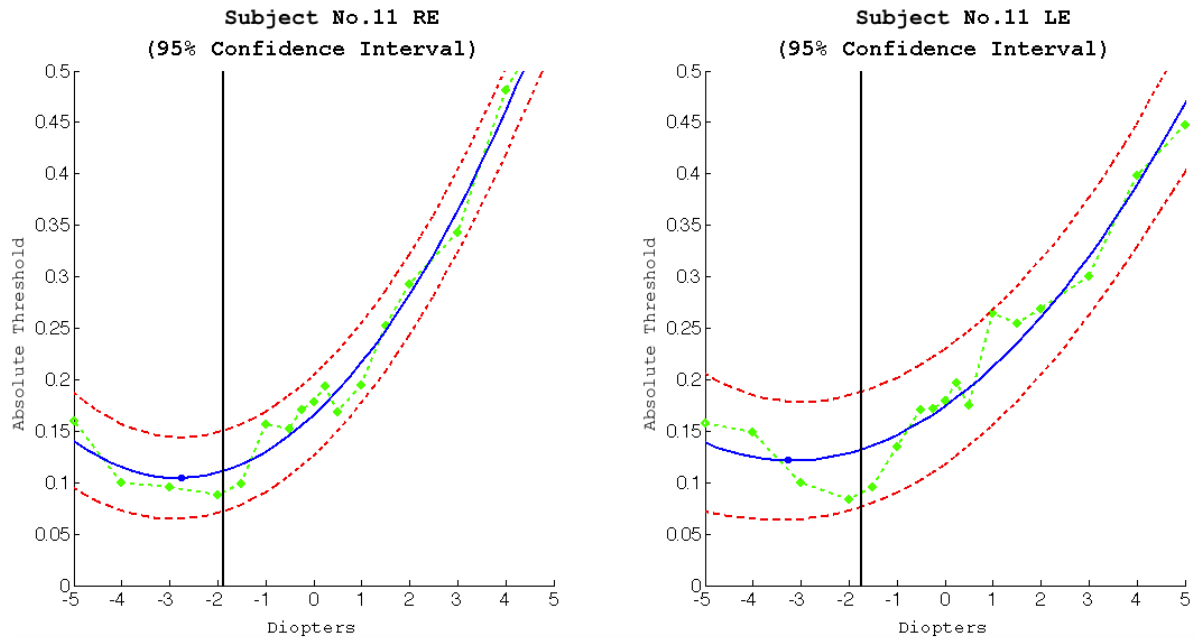
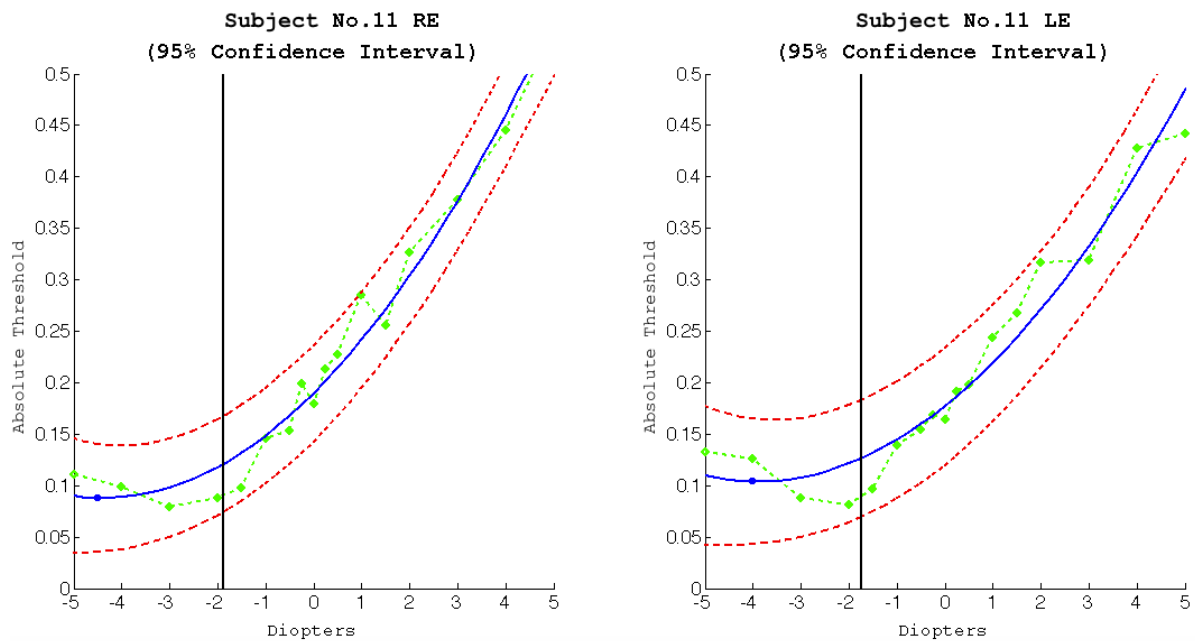


Figure 5.7 – Polynomial fitting of the absolute threshold values of Individual 1. Red lines define the confidence interval of 95%. Green plot points the minimum value for a specific extra lens power, and the blue lines represent the best polynomial fitting highlighting its minor value.



(a) with eye drops



(b) without eye drops

Figure 5.8 – Polynomial fitting of the absolute threshold values of Individual 11. Red lines define the confidence interval of 95%. Green plot points the minimum value for a specific extra lens power, and the blue lines represent the best polynomial fitting highlighting its minor value.



## 6 CONCLUSION

This thesis presented a practical approach to the problem of visual simulation of [blur](#) on monochromatic images. Our approach uses Fourier tools and a camera to simulate and validate results of how low-order aberrations affect vision. Even though that results seems to be visually correct, we've adopted two objective metrics to compare our results with the optical ground truth. In addition, this thesis has demonstrated the results of psychophysical studies of the absolute threshold. However, due to the crystalline lens involuntary accommodation, this intrinsic characteristic cannot be used to estimate the spherical equivalent refraction.

Although our solution is able to take into account the individual's refractive high-order aberrations, our focus is on not relying on the availability of expensive equipment, such as Shack-Hartmann wavefront sensors. For this, we estimate the low-order-aberration components of the individual's PSFs directly from his/her eyeglasses or contact lenses prescriptions, and use them to simulate the perception of Sloan letters. Given its reduced input need, our technique can help doctors, patients, and teachers to experiment the visual complaints.

### 6.1 Future Work

Because visual blurring is a depth-dependent phenomenon, we would like to capture image and depth information from the environment and generate real-time simulations of how low-order aberrations affect the perception of it. Also, we suppose that, by assuming additional information from the individuals in simulations (*e.g.*, absolute threshold), the final result could be hugely improved. In a way that, for example, we could generate images or design displays focusing on intrinsic perception or higher-order optical aberration, which cannot be corrected with ordinary eyeglasses.

It would be interesting to study the best objective metric to compare results. Also, for qualitative validation, we could simulate the vision of a number of individuals who use eyeglasses. And ask the subjects to observe several scenes without using their eyeglasses, as well as to observe the simulated views with eyeglasses on. By doing this, they could indicate how well the simulation approximates their actual vision.





## REFERENCES

- BAILEY, I.; LOVIE, J. New design principles for visual acuity letter charts. **American journal of optometry and physiological optics**, v. 53, n. 11, p. 740—745, November 1976. ISSN 0093-7002. Available from Internet: <<http://europepmc.org/abstract/MED/998716>>.
- BARSKY, B. A. Vision-realistic rendering: Simulation of the scanned foveal image from wavefront data of human subjects. In: **Proceedings of the 1st Symposium on Applied Perception in Graphics and Visualization**. New York, NY, USA: ACM, 2004. (APGV '04), p. 73–81. ISBN 1-58113-914-4. Available from Internet: <<http://doi.acm.org/10.1145/1012551.1012564>>.
- BLAKE, R.; SEKULER, R. **Perception**. 5. ed. New York, NY, USA: McGraw-Hill Humanities/Social Sciences/Languages, 2005.
- CAMP, J.; MAGUIRE, L.; ROBB, R. An efficient ray tracing algorithm for modeling visual performance from corneal topography. In: **Visualization in Biomedical Computing, 1990., Proceedings of the First Conference on**. [S.l.: s.n.], 1990. p. 278–285.
- DAI, G.-m. **Wavefront Optics for Vision Correction**. Bellingham, Washington USA: SPIE PRESS, 2008.
- DEERING, M. F. A photon accurate model of the human eye. **ACM Trans. Graph.**, ACM, New York, NY, USA, v. 24, n. 3, p. 649–658, jul 2005. ISSN 0730-0301. Available from Internet: <<http://doi.acm.org/10.1145/1073204.1073243>>.
- DIAS-SANTOS, A. et al. Higher order aberrations in amblyopic children and their role in refractory amblyopia. **Revista Brasileira de Oftalmologia**, SciELO Brasil, v. 73, p. 358–362, 12 2014. ISSN 0034-7280. Available from Internet: <[http://www.scielo.br/scielo.php?script=sci\\_arttext&pid=S0034-72802014000600358&nrm=iso](http://www.scielo.br/scielo.php?script=sci_arttext&pid=S0034-72802014000600358&nrm=iso)>.
- GLYTISIS, E. N. Example of a simple optical system. Class Note. 2014.
- GOODMAN, J. W. **Introduction to Fourier optics**. 3. ed. Englewood: Roberts and Company Publishers, 2005.
- HUANG, F.-C. et al. Correcting for optical aberrations using multilayer displays. **ACM Trans. Graph.**, ACM, New York, NY, USA, v. 31, n. 6, p. 185:1–185:12, nov 2012. ISSN 0730-0301. Available from Internet: <<http://doi.acm.org/10.1145/2366145.2366204>>.
- HUANG, F.-C. et al. Eyeglasses-free display: Towards correcting visual aberrations with computational light field displays. **ACM Trans. Graph.**, ACM, New York, NY, USA, v. 33, n. 4, p. 59:1–59:12, jul. 2014. ISSN 0730-0301. Available from Internet: <<http://doi.acm.org/10.1145/2601097.2601122>>.
- KING, L. A. **Experience Psychology**. 2. ed. [S.l.]: McGraw-Hill Education, 2012.
- KLEIN, S. A. Measuring, estimating, and understanding the psychometric function: a commentary. **Perception & Psychophysics**, v. 63, p. 1421–1455, 2001.

KOLB, C.; MITCHELL, D.; HANRAHAN, P. A realistic camera model for computer graphics. In: **Proceedings of the 22Nd Annual Conference on Computer Graphics and Interactive Techniques**. New York, NY, USA: ACM, 1995. (SIGGRAPH '95), p. 317–324. ISBN 0-89791-701-4. Available from Internet: <<http://doi.acm.org/10.1145/218380.218463>>.

KRONBAUER, A. L. et al. Vision measurement in candelas: description of a psychophysical technique to quantify luminous intensity. **Arquivos brasileiros de oftalmologia**, v. 74, n. 2, p. 91–96, 2011. ISSN 0004-2749. Available from Internet: <<http://dx.doi.org/10.1590/S0004-27492011000200004>>.

LEEK, M. R. Adaptive procedures in psychophysical research. **Perception & Psychophysics**, v. 63, n. 8, p. 1279–1292, 2001.

LEMMA, G. General psychology. Lecture Notes. 2005.

LIANG, J. et al. Objective measurement of wave aberrations of the human eye with the use of a hartmann–shack wave-front sensor. **J. Opt. Soc. Am. A**, OSA, v. 11, n. 7, p. 1949–1957, Jul 1994. Available from Internet: <<http://josaa.osa.org/abstract.cfm?URI=josaa-11-7-1949>>.

MACHADO, G. M.; OLIVEIRA, M.; FERNANDES, L. A. A physiologically-based model for simulation of color vision deficiency. **Visualization and Computer Graphics, IEEE Transactions on**, v. 15, n. 6, p. 1291–1298, Nov 2009. ISSN 1077-2626.

MOLLON, J. **The origins of modern color science**. 2. ed. Oxford, UK: Elsevier, 2003.

MONTALTO, C. et al. A total variation approach for customizing imagery to improve visual acuity. **ACM Trans. Graph.**, ACM, New York, NY, USA, v. 34, n. 3, p. 28:1–28:16, may 2015. ISSN 0730-0301. Available from Internet: <<http://doi.acm.org/10.1145/2717307>>.

MOSTAFAWY, S.; KERMANI, O.; LUBATSCHOWSKI, H. Virtual eye: retinal image visualization of the human eye. **Computer Graphics and Applications, IEEE**, v. 17, n. 1, p. 8–12, Jan 1997. ISSN 0272-1716.

PAMPLONA, V. F. et al. Netra: Interactive display for estimating refractive errors and focal range. **ACM Trans. Graph.**, ACM, New York, NY, USA, v. 29, n. 4, p. 77:1–77:8, 7 2010. ISSN 0730-0301. Available from Internet: <<http://doi.acm.org/10.1145/1778765.1778814>>.

PAMPLONA, V. F. et al. Tailored displays to compensate for visual aberrations. **ACM Trans. Graph.**, v. 31, n. 4, p. 81, 2012.

PAMPLONA, V. F.; OLIVEIRA, M. M.; BARANOSKI, G. V. G. Photorealistic models for pupil light reflex and iridal pattern deformation. **ACM Trans. Graph.**, ACM, New York, NY, USA, v. 28, n. 4, p. 106:1–106:12, sep 2009. ISSN 0730-0301. Available from Internet: <<http://doi.acm.org/10.1145/1559755.1559763>>.

PAMPLONA, V. F. et al. Catra: Interactive measuring and modeling of cataracts. In: **ACM SIGGRAPH 2011 Papers**. New York, NY, USA: ACM, 2011. (SIGGRAPH '11), p. 47:1–47:8. ISBN 978-1-4503-0943-1. Available from Internet: <<http://doi.acm.org/10.1145/1964921.1964942>>.

PELLI, D.; ROBSON, J. et al. The design of a new letter chart for measuring contrast sensitivity. In: **Clinical Vision Sciences**. [S.l.]: Raphael's Ltd, London, 1988.

POTMESIL, M.; CHAKRAVARTY, I. A lens and aperture camera model for synthetic image generation. **ACM SIGGRAPH Computer Graphics**, ACM, v. 15, n. 3, p. 297–305, 1981.

RITSCHHEL, T. et al. Temporal glare: Real-time dynamic simulation of the scattering in the human eye. **Computer Graphics Forum**, Blackwell Publishing Ltd, v. 28, n. 2, p. 183–192, 2009. ISSN 1467-8659. Available from Internet: <<http://dx.doi.org/10.1111/j.1467-8659.2009.01357.x>>.

SACEK, V. **Monochromatic Eye Aberrations**. 2015. Available from Internet: <[http://www.telescope-optics.net/monochromatic\\_eye\\_aberrations.htm](http://www.telescope-optics.net/monochromatic_eye_aberrations.htm)>.

SCHWARTZ, S. H. **Visual perception: A clinical orientation**. 4. ed. New York, NY, USA: McGraw-Hill Medical Pub. Division, 2010.

SCHWIEGERLING, J. **Field Guide to Visual and Ophthalmic Optics**. [S.l.]: SPIE press Bellingham, WA, 2004. (SPIE Field Guides, FG04).

SMITH, A. **PSFs in IDL**. 2015. Available from Internet: <<http://www.enkaptic.co.uk/2009/03/18/psfs-in-idl/>>.

THIBOS, L. N. et al. Standards for reporting the optical aberrations of eyes. **Journal of refractive surgery**, Slack Incorporated, v. 18, n. 5, p. S652–S660, 2002.

THIBOS, L. N.; THIBOS, C. A. Geometrical optical analysis of defocused retinal images to compute the size of retinal blur circles relative to object size. **US Ophthalmic Review**, v. 4, n. 2, p. 104–106, 7 2011.

TKACZYK, T. S. **Field Guide to Microscopy**. [S.l.]: SPIE press Bellingham, WA, 2010. (SPIE Field Guides, FG13).

TREUTWEIN, B. Adaptive psychophysical procedures. **Vision Research**, v. 17, n. 1503-2522, 1995.

WATSON, A. B.; AHUMADA JR, A. J. Predicting visual acuity from wavefront aberrations. **Journal of Vision**, v. 8, n. 4, p. 17, 2008. Available from Internet: <<http://dx.doi.org/10.1167/8.4.17>>.

WHO. **Global Initiative for the Elimination of Avoidable Blindness: action plan 2006-2011**. [S.l.], 2007.

YODER, P. R.; VUKOBRATOVICH, D. **Field Guide to Binoculars and Scopes**. [S.l.]: SPIE press Bellingham, WA, 2011. (SPIE Field Guides, FG19).

YU, W. M. **Simulation of Vision through an Actual Human Optical System**. Thesis (PhD) — University of California, Berkeley, 2001.

ZIMBARDO, P. G.; JOHNSON, R. L.; MCCANN, V. **Psychology: core concepts**. 7. ed. New York, NY, USA: Pearson Education, 2012.



## APPENDIX A — INDIVIDUAL PARTICIPANT DATA

This appendix contains data captured through the experiments described in Section 5.1.1. The following participant data is related to the subject with ID number 001. The complete database describing the results can be downloaded at:

**[http://www.inf.ufrgs.br/~mlkrueger/MSc\\_Dissertation/IPD\\_Database.zip](http://www.inf.ufrgs.br/~mlkrueger/MSc_Dissertation/IPD_Database.zip)**

### **ID Number**

Subject identification number

### **REF. DATA**

Examination reference data

### **EYE DROPS**

Whether cycloplegic eye drop was used or not

### **VD**

Vertex distance configured in the TOPCON KR-8900 Autorefractor device

### **CYL**

Cylinder notation (Brazilian notation is the negative one)

### **PD**

Pupil distance

### **S**

Spherical

### **C**

Cylindrical

### **A**

Cylindrical axis

### **S.E.**

Spherical Equivalent ( $SE = S + (C/2)$ )

### **MV**

Minimum visible

### **ET**

Elapsed time

### **LM**

Lux Mean



## IPD - Individual Participant Data

ID Number: 001

Birthdate: 13/03/1990

Gender: Male

KR-8900

TOPCON

REF. DATA		27/11/2014	
EYE DROPS		[X] YES [ ] NO	
VD	CYL	PD	
12.00	(-)	61	
< RIGHT EYE >			
S	C	A	S.E.
+ 1,25	- 0,25	7	+ 1,13
< LEFT EYE >			
S	C	A	S.E.
+ 1,25	0,00	0	+ 1,25

REF. DATA		27/11/2014	
EYE DROPS		[ ] YES [X] NO	
VD	CYL	PD	
12.00	(-)	61	
< RIGHT EYE >			
S	C	A	S.E.
+ 0,50	- 0,25	6	+ 0,38
< LEFT EYE >			
S	C	A	S.E.
+ 0,75	- 0,25	2	+ 0,63

### MATLAB Random Sequences

1st Examination	2nd Examination	3rd Examination	4th Examination
- 1,50	+ 1,50	- 0,25	+ 3,00
+ 1,00	+ 4,00	- 3,00	+ 2,00
+ 1,50	- 0,50	+ 1,00	+ 1,50
- 4,00	- 4,00	- 2,00	- 0,50
- 0,50	+ 1,00	- 5,00	- 1,50
0,00	- 0,25	+ 3,00	0,00
- 1,00	- 1,50	+ 1,50	- 3,00
+ 3,00	+ 0,50	+ 0,25	+ 5,00
- 2,00	+ 2,00	- 4,00	- 0,25
+ 0,50	- 1,00	+ 4,00	- 5,00
+ 2,00	0,00	+ 5,00	- 4,00
- 3,00	+ 5,00	- 0,50	+ 0,25
+ 4,00	+ 3,00	+ 0,50	+ 1,00
+ 5,00	- 2,00	+ 2,00	- 1,00
+ 0,25	+ 0,25	- 1,50	+ 0,50
- 0,25	- 5,00	0,00	- 2,00
- 5,00	- 3,00	- 1,00	+ 4,00



## IPD - Individual Participant Data

ID Number: 001

Birthdate: 13/03/1990

Gender: Male

REF. DATA: 27/11/2014

EYE DROPS: YES

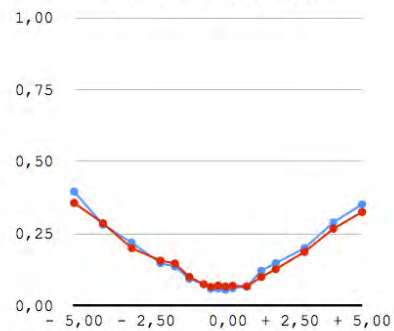
DURATION: 15m 39s

### 1st Examination

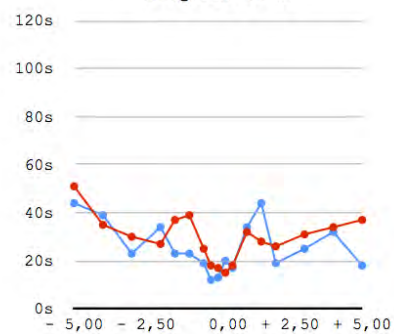
Dioptr	Eye	MV	ET	LM
+ 5,00	<R>	0,3522	18s	338 lx
	<L>	0,3256	37s	337 lx
+ 4,00	<R>	0,2894	32s	333 lx
	<L>	0,2674	34s	333 lx
+ 3,00	<R>	0,2000	25s	337 lx
	<L>	0,1872	31s	337 lx
+ 2,00	<R>	0,1481	19s	337 lx
	<L>	0,1271	26s	337 lx
+ 1,50	<R>	0,1215	44s	346 lx
	<L>	0,1000	28s	339 lx
+ 1,00	<R>	0,0669	34s	340 lx
	<L>	0,0674	32s	340 lx
+ 0,50	<R>	0,0611	17s	339 lx
	<L>	0,0696	18s	338 lx
+ 0,25	<R>	0,0553	20s	337 lx
	<L>	0,0674	15s	338 lx
0,00	<R>	0,0601	13s	343 lx
	<L>	0,0703	17s	340 lx
- 0,25	<R>	0,0592	12s	339 lx
	<L>	0,0655	18s	339 lx
- 0,50	<R>	0,0744	19s	345 lx
	<L>	0,0749	25s	341 lx
- 1,00	<R>	0,0940	23s	341 lx
	<L>	0,1000	39s	339 lx
- 1,50	<R>	0,1365	23s	337 lx
	<L>	0,1471	37s	336 lx
- 2,00	<R>	0,1478	34s	337 lx
	<L>	0,1568	27s	339 lx
- 3,00	<R>	0,2193	23s	334 lx
	<L>	0,2000	30s	334 lx
- 4,00	<R>	0,2821	39s	350 lx
	<L>	0,2867	35s	351 lx
- 5,00	<R>	0,3966	44s	339 lx
	<L>	0,3572	51s	337 lx

<R> <L>

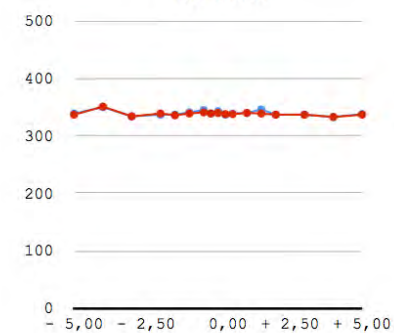
### Minimum Visible



### Elapsed Time



### Lux Mean





## IPD - Individual Participant Data

ID Number: 001

Birthdate: 13/03/1990

Gender: Male

REF. DATA: 11/11/2014

EYE DROPS: NO

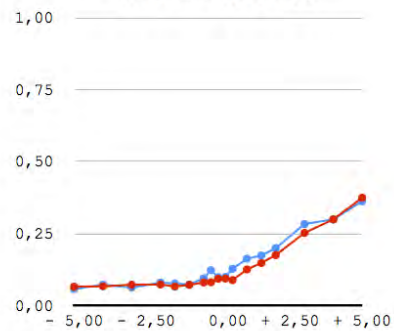
DURATION: 17m 8s

### 2nd Examination

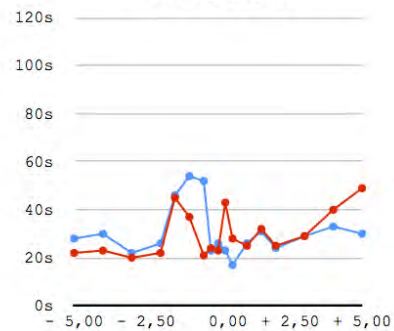
Dioptr	Eye	MV	ET	LM
+ 5,00	<R>	0,3628	30s	233 lx
	<L>	0,3751	49s	235 lx
+ 4,00	<R>	0,3000	33s	231 lx
	<L>	0,3000	40s	232 lx
+ 3,00	<R>	0,2838	29s	234 lx
	<L>	0,2531	29s	232 lx
+ 2,00	<R>	0,2000	24s	233 lx
	<L>	0,1761	25s	232 lx
+ 1,50	<R>	0,1744	31s	236 lx
	<L>	0,1486	32s	232 lx
+ 1,00	<R>	0,1635	26s	232 lx
	<L>	0,1261	25s	232 lx
+ 0,50	<R>	0,1285	17s	232 lx
	<L>	0,0891	28s	229 lx
+ 0,25	<R>	0,1000	23s	231 lx
	<L>	0,0944	43s	235 lx
0,00	<R>	0,0990	26s	231 lx
	<L>	0,0937	23s	229 lx
- 0,25	<R>	0,1237	23s	231 lx
	<L>	0,0816	24s	231 lx
- 0,50	<R>	0,0954	52s	234 lx
	<L>	0,0809	21s	232 lx
- 1,00	<R>	0,0737	54s	233 lx
	<L>	0,0727	37s	233 lx
- 1,50	<R>	0,0775	46s	234 lx
	<L>	0,0667	45s	226 lx
- 2,00	<R>	0,0804	26s	231 lx
	<L>	0,0739	22s	233 lx
- 3,00	<R>	0,0630	22s	232 lx
	<L>	0,0732	20s	233 lx
- 4,00	<R>	0,0734	30s	234 lx
	<L>	0,0674	23s	232 lx
- 5,00	<R>	0,0580	28s	233 lx
	<L>	0,0664	22s	232 lx

◊ <R> ◊ <L>

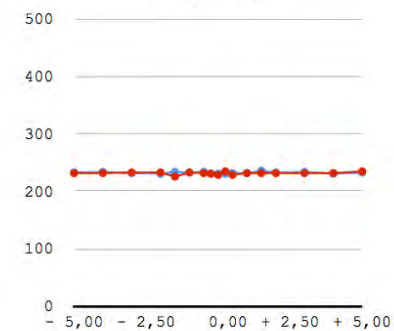
### Minimum Visible



### Elapsed Time



### Lux Mean







## IPD - Individual Participant Data

ID Number: 001

Birthdate: 13/03/1990

Gender: Male

REF. DATA: 13/11/2014

EYE DROPS: NO

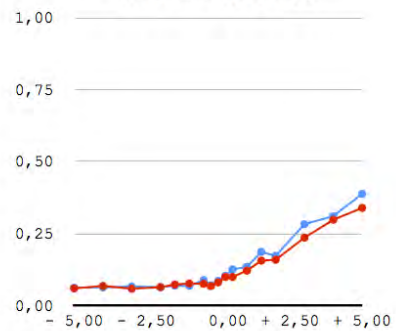
DURATION: 13m 56s

### 3rd Examination

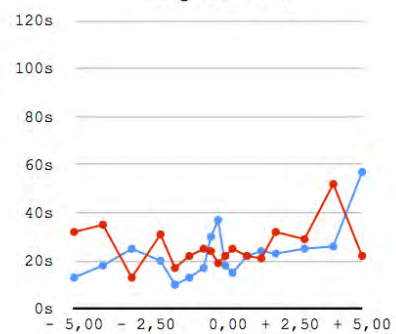
Dioptr	Eye	MV	ET	LM
+ 5,00	<R>	0,3886	57s	251 lx
	<L>	0,3399	22s	251 lx
+ 4,00	<R>	0,3114	26s	257 lx
	<L>	0,2986	52s	253 lx
+ 3,00	<R>	0,2836	25s	258 lx
	<L>	0,2367	29s	255 lx
+ 2,00	<R>	0,1734	23s	256 lx
	<L>	0,1599	32s	251 lx
+ 1,50	<R>	0,1870	24s	253 lx
	<L>	0,1568	21s	252 lx
+ 1,00	<R>	0,1353	22s	250 lx
	<L>	0,1220	22s	251 lx
+ 0,50	<R>	0,1263	15s	256 lx
	<L>	0,1000	25s	256 lx
+ 0,25	<R>	0,1036	18s	252 lx
	<L>	0,1000	22s	253 lx
0,00	<R>	0,0862	37s	253 lx
	<L>	0,0812	19s	256 lx
- 0,25	<R>	0,0710	30s	249 lx
	<L>	0,0681	24s	250 lx
- 0,50	<R>	0,0894	17s	256 lx
	<L>	0,0761	25s	254 lx
- 1,00	<R>	0,0686	13s	255 lx
	<L>	0,0775	22s	258 lx
- 1,50	<R>	0,0703	10s	252 lx
	<L>	0,0739	17s	250 lx
- 2,00	<R>	0,0645	20s	251 lx
	<L>	0,0645	31s	252 lx
- 3,00	<R>	0,0671	25s	252 lx
	<L>	0,0594	13s	251 lx
- 4,00	<R>	0,0638	18s	258 lx
	<L>	0,0688	35s	258 lx
- 5,00	<R>	0,0626	13s	258 lx
	<L>	0,0604	32s	259 lx

<R> <L>

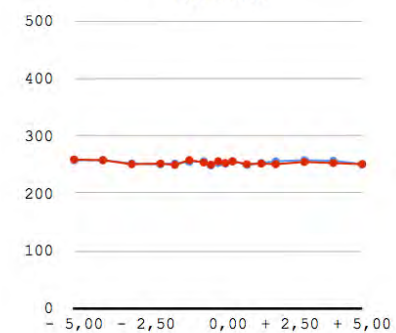
#### Minimum Visible



#### Elapsed Time



#### Lux Mean





## IPD - Individual Participant Data

ID Number: 001

Birthdate: 13/03/1990

Gender: Male

REF. DATA: 14/11/2014

EYE DROPS: NO

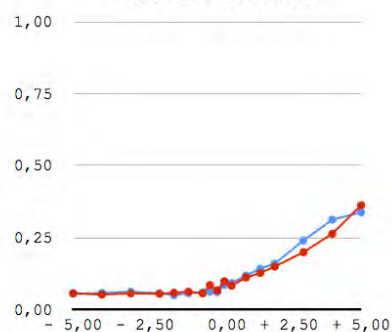
DURATION: 10m 23s

### 4th Examination

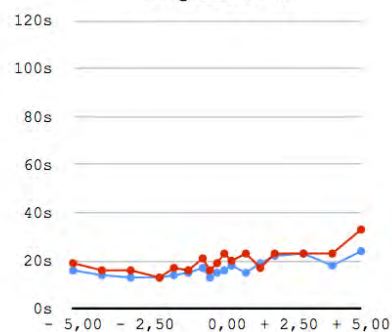
Dioptr	Eye	MV	ET	LM
+ 5,00	<R>	0,3384	24s	245 lx
	<L>	0,3628	33s	246 lx
+ 4,00	<R>	0,3128	18s	250 lx
	<L>	0,2640	23s	249 lx
+ 3,00	<R>	0,2408	23s	244 lx
	<L>	0,2000	23s	242 lx
+ 2,00	<R>	0,1601	22s	242 lx
	<L>	0,1500	23s	243 lx
+ 1,50	<R>	0,1428	19s	242 lx
	<L>	0,1278	17s	241 lx
+ 1,00	<R>	0,1186	15s	246 lx
	<L>	0,1118	23s	245 lx
+ 0,50	<R>	0,0928	18s	246 lx
	<L>	0,0838	20s	246 lx
+ 0,25	<R>	0,0870	16s	247 lx
	<L>	0,0988	23s	247 lx
0,00	<R>	0,0611	15s	243 lx
	<L>	0,0674	19s	242 lx
- 0,25	<R>	0,0628	13s	244 lx
	<L>	0,0855	16s	242 lx
- 0,50	<R>	0,0606	17s	243 lx
	<L>	0,0570	21s	243 lx
- 1,00	<R>	0,0575	15s	246 lx
	<L>	0,0628	16s	244 lx
- 1,50	<R>	0,0510	14s	243 lx
	<L>	0,0589	17s	242 lx
- 2,00	<R>	0,0570	13s	247 lx
	<L>	0,0556	13s	246 lx
- 3,00	<R>	0,0626	13s	244 lx
	<L>	0,0568	16s	243 lx
- 4,00	<R>	0,0580	14s	246 lx
	<L>	0,0527	16s	245 lx
- 5,00	<R>	0,0560	16s	245 lx
	<L>	0,0572	19s	243 lx

◊ <R> ◊ <L>

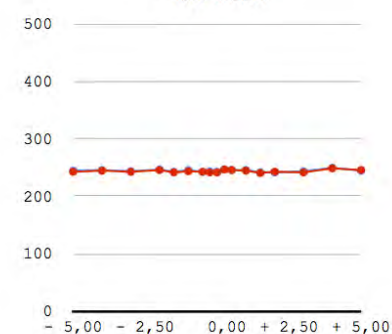
### Minimum Visible



### Elapsed Time



### Lux Mean





## IPD - Individual Participant Data

**ID Number:** 001

*Analysis of the data captured without eye drops*

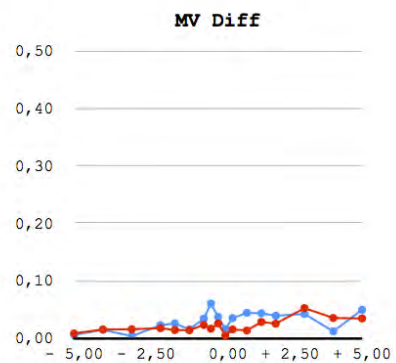
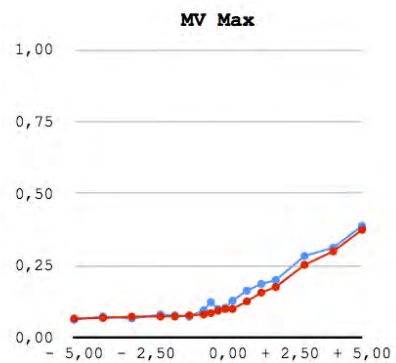
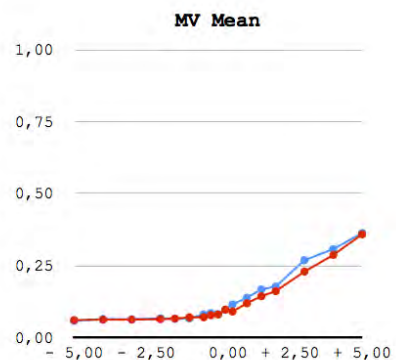
**Birthdate:** 13/03/1990

**Gender:** Male

### Minimum Visible

Dioptr	Eye	Mean	Max	Diff
+ 5,00	<R>	0,3633	0,3886	0,0502
	<L>	0,3593	0,3751	0,0352
+ 4,00	<R>	0,3081	0,3128	0,0128
	<L>	0,2875	0,3000	0,0360
+ 3,00	<R>	0,2694	0,2838	0,0430
	<L>	0,2299	0,2531	0,0531
+ 2,00	<R>	0,1778	0,2000	0,0399
	<L>	0,1620	0,1761	0,0261
+ 1,50	<R>	0,1681	0,1870	0,0442
	<L>	0,1444	0,1568	0,0290
+ 1,00	<R>	0,1391	0,1635	0,0449
	<L>	0,1200	0,1261	0,0143
+ 0,50	<R>	0,1159	0,1285	0,0357
	<L>	0,0910	0,1000	0,0162
+ 0,25	<R>	0,0969	0,1036	0,0166
	<L>	0,0977	0,1000	0,0056
0,00	<R>	0,0821	0,0990	0,0379
	<L>	0,0808	0,0937	0,0263
- 0,25	<R>	0,0858	0,1237	0,0609
	<L>	0,0784	0,0855	0,0174
- 0,50	<R>	0,0818	0,0954	0,0348
	<L>	0,0713	0,0809	0,0239
- 1,00	<R>	0,0666	0,0737	0,0162
	<L>	0,0710	0,0775	0,0147
- 1,50	<R>	0,0663	0,0775	0,0265
	<L>	0,0665	0,0739	0,0150
- 2,00	<R>	0,0673	0,0804	0,0234
	<L>	0,0647	0,0739	0,0183
- 3,00	<R>	0,0642	0,0671	0,0045
	<L>	0,0631	0,0732	0,0164
- 4,00	<R>	0,0651	0,0734	0,0154
	<L>	0,0630	0,0688	0,0161
- 5,00	<R>	0,0589	0,0626	0,0066
	<L>	0,0613	0,0664	0,0092

◊ <R> ◊ <L>







## ANNEX A — EXAMPLE OF A SIMPLE OPTICAL SYSTEM

### EXAMPLE OF A SIMPLE OPTICAL SYSTEM<sup>†</sup>

A system of two thin lenses is given as shown in Fig. 1. The left thin lens has a focal distance of  $f_1 = 50$  mm (converging) and the right thin lens has a focal distance of  $f_2 = 25$  mm (converging also). The two thin lenses are separated by 40 mm. An object is placed at a distance of 75 mm to the left of the left thin lens. Find the position and magnification of the final image using (a) the method of matrices, (b) the thin lens equation, and (c) the method of the cardinal points.

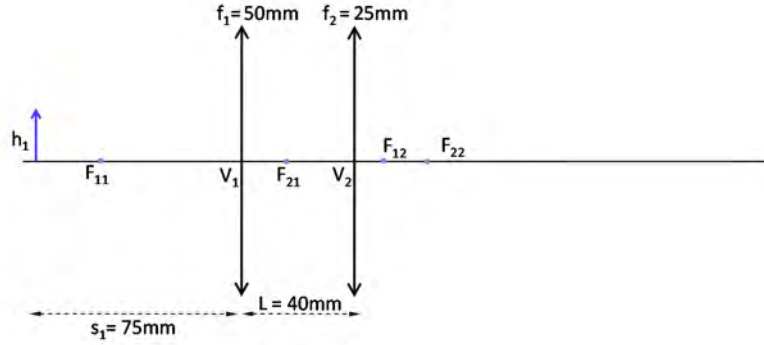


Figure 1: The optical system consisting of two thin-lenses of focal distances of 50mm and 25mm respectively, separated by a distance of 40mm.

#### A. Method of ABCD Matrices

The matrix ABCD of the two thin lenses separated by a distance  $L = 40$  mm can be determined by the multiplication of three basic ABCD matrices, the right thin lens matrix, the propagation by distance  $L$  matrix, and the left thin lens matrix. Multiplying the three matrices the ABCD of the optical system comprising of the two thin lenses can be calculated as follows:

$$\begin{bmatrix} A_{TL} & B_{TL} \\ C_{TL} & D_{TL} \end{bmatrix} = \begin{bmatrix} 1 & 0 \\ -\frac{1}{25} & 1 \end{bmatrix} \begin{bmatrix} 1 & 40 \\ 0 & 1 \end{bmatrix} \begin{bmatrix} 1 & 0 \\ -\frac{1}{50} & 1 \end{bmatrix} = \begin{bmatrix} 0.20 & 40 \text{ mm} \\ -0.028 \text{ mm}^{-1} & -0.6 \end{bmatrix}. \quad (1)$$

Now it is assumed that the image is formed at a distance  $x$  to the right of the right thin lens. Then if the object plane is considered as the input plane and the image plane as the output plane of the overall optical system, the overall ABCD matrix can be determined as follows (see Figure 2):

<sup>†</sup>written by Prof. Elias N. Glytsis, Last Update: May 29, 2014

$$\begin{bmatrix} A & B \\ C & D \end{bmatrix} = \begin{bmatrix} 1 & x \\ 0 & 1 \end{bmatrix} \begin{bmatrix} A_{TL} & B_{TL} \\ C_{TL} & D_{TL} \end{bmatrix} \begin{bmatrix} 1 & 75 \\ 0 & 1 \end{bmatrix} = \begin{bmatrix} 0.20 - 0.028x & 55 - 2.7x(mm) \\ -0.028 mm^{-1} & 2.7 \end{bmatrix}. \quad (2)$$

In order to achieve image formation it is necessary for the overall ABCD matrix element  $B$  to become zero. When  $B = 0$  the value of  $A$  gives the overall magnification of the image. Therefore,

$$B = 0 \implies 55 - 2.7x = 0 \implies x = 20.37 mm, \quad (3)$$

while the magnification,  $m$ , is given by

$$m = A(x = 20.37) = 0.2 - 0.028x = -0.37. \quad (4)$$

Therefore, the image is real and inverted.

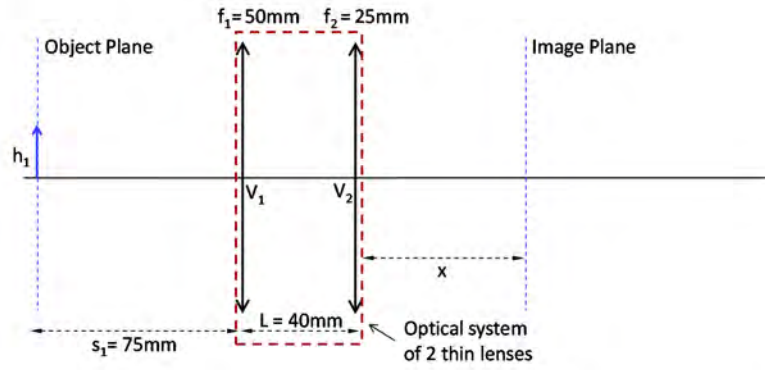


Figure 2: The optical system consisting of two thin-lenses of focal distances of 50mm and 25mm respectively, separated by a distance of 40mm is represented by the dashed rectangle and an equivalent ABCD matrix. The image plane is considered to be at the unknown distance  $x$  away from the right thin lens.

## B. Method of Thin Lenses

In this approach the thin lens equation is used sequentially for each lens. First the thin lens equation is applied for the left lens. The object distance  $s_1 = 75\text{mm}$  and the focal distance  $f_1 = +50\text{mm}$ . Applying the thin lens equation in this case the image distance,  $s'_1$  due to the first lens (if the second lens is temporarily neglected) can be determined from the equation

$$\frac{1}{s_1} + \frac{1}{s'_1} = \frac{1}{f_1} \implies \frac{1}{75} + \frac{1}{s'_1} = \frac{1}{50} \implies s'_1 = 150 mm. \quad (5)$$

The image formed by the first lens serves as the object for the second (right) lens. Since the image is to the right of the right lens it will serve as a virtual object for the second lens. Therefore,  $s_2 = -(150 - 40) = -110$  mm. Applying the thin lens equation for the second lens the final image location can be determined.

$$\frac{1}{s_2} + \frac{1}{s'_2} = \frac{1}{f_2} \Rightarrow \frac{1}{-110} + \frac{1}{s'_2} = \frac{1}{25} \Rightarrow s'_2 = 20.37 \text{ mm}. \quad (6)$$

Therefore, the final image is formed 20.37 mm to the right of the right lens and is a real image. The magnification can be found as follows

$$m = \frac{h'_2}{h_1} = \frac{h'_1}{h_1} \frac{h'_2}{h_2} = \left(-\frac{s'_1}{s_1}\right) \left(-\frac{s'_2}{s_2}\right) = -\frac{150}{75} \left(-\frac{20.37}{-110}\right) = -0.37, \quad (7)$$

implying the the final image is inverted (and real as it was determined through  $s'_2$ ). A ray diagram of the image formation by the two lenses is shown in Fig. 3.

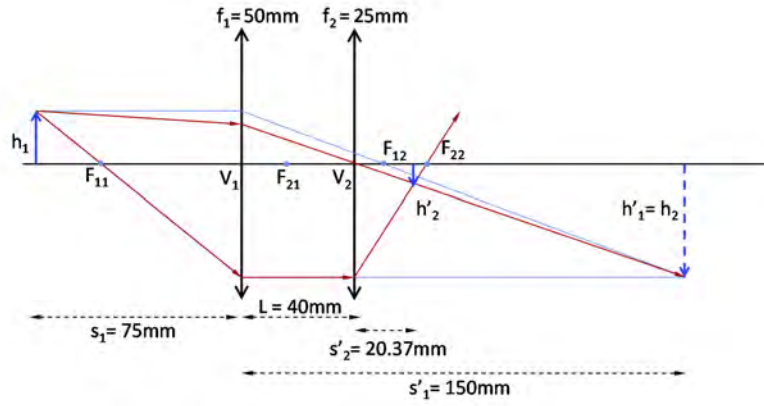


Figure 3: A rays diagram for the two-lenses system.

### C. Method of Cardinal Points

In order to determine the cardinal points ( $H_1 \equiv N_1$ ,  $H_2 \equiv N_2$ ,  $F_1$ , and  $F_2$ ), the matrix ABCD of the optical system comprised of the two thin lenses must be used. This matrix was computed earlier and is equal to

$$\begin{bmatrix} A_{TL} & B_{TL} \\ C_{TL} & D_{TL} \end{bmatrix} = \begin{bmatrix} 0.20 & 40 \text{ mm} \\ -0.028 \text{ mm}^{-1} & -0.6 \end{bmatrix}. \quad (8)$$

Using the elements of the matrix the signed distances,  $f_1$ ,  $f_2$ ,  $r$ , and  $s$  (see Fig. 4) can be determined as follows:

$$f_1 = \frac{n_0/n_f}{C_{TL}} = \frac{1}{-0.028} = -35.714 \text{ mm}, \quad (9)$$

$$f_2 = -\frac{1}{C_{TL}} = -\frac{1}{-0.028} = +35.714 \text{ mm}, \quad (10)$$

$$r = \frac{D_{TL} - (n_0/n_f)}{C_{TL}} = \frac{-0.6 - 1}{-0.028} = +57.1428 \text{ mm}, \quad (11)$$

$$s = \frac{1 - A_{TL}}{C_{TL}} = \frac{1 - 0.2}{-0.028} = -28.5714 \text{ mm}, \quad (12)$$

Now the thin lens equation can be used by suitably choosing the object and image distances  $s_o$  and  $s_i$  by measuring them from the first and the second principal planes respectively. For this case  $s_o = 75 + r = 132.1428 \text{ mm}$ . The focal distance of the system is  $f = 35.714 \text{ mm}$ . Then the thin lens equation can be written as follows

$$\frac{1}{s_o} + \frac{1}{s_i} = \frac{1}{f} \Rightarrow \frac{1}{132.1428} + \frac{1}{s_i} = \frac{1}{35.714} \Rightarrow s_i = 48.9412 \text{ mm}. \quad (13)$$

Therefore the position of the real image ( $s_i > 0$ ) from the right thin lens is  $s_i - |s| = 48.9412 - 28.5714 = 20.37 \text{ mm}$ . The magnification is  $m = -s_i/s_o = -48.9412/132.1428 = -0.37$  as it was computed and with the other methods. A ray diagram using the cardinal points is shown in Fig. 5.

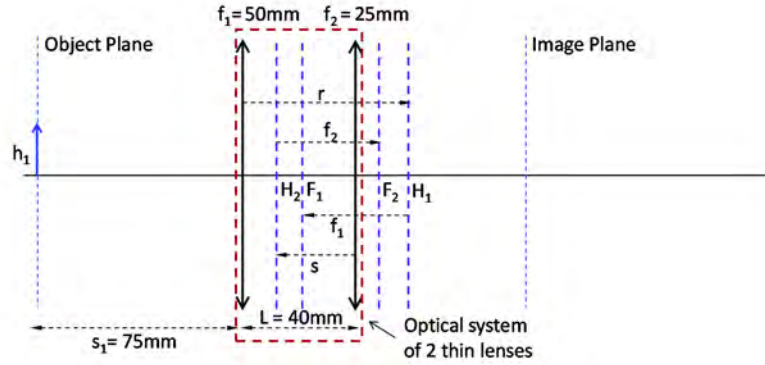


Figure 4: Important distances for the determination of the cardinal points of the two lenses optical system. The nodal points  $N_1$  and  $N_2$  coincide with the principal points  $H_1$  and  $H_2$  respectively.



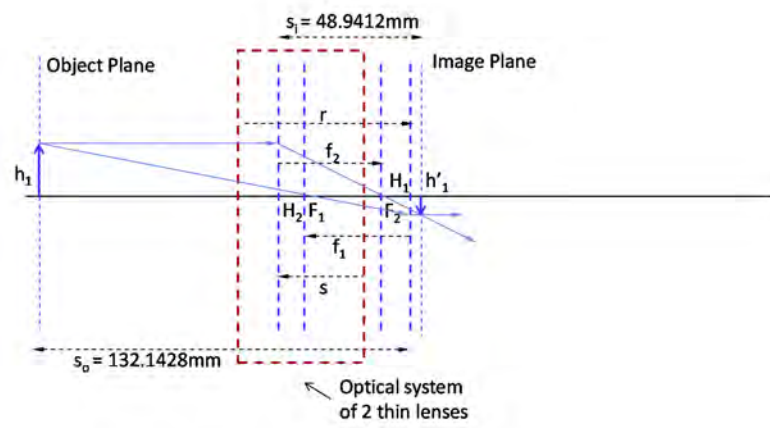


Figure 5: A rays diagram that shows the formation of the image through the use of the cardinal points of the two lenses system.